Statistical analysis of the interplay between interstellar magnetic fields and filaments hosting Planck Galactic cold clumps

D. Alina, I. Ristorcelli, L. Montier, E Abdikamalov, M. Juvela, K. Ferrière, J-Ph Bernard, E Micelotta

Monthly Notices
of the
ROYAL ASTRONOMICAL SOCIETY

MNRAS **485,** 2825–2843 (2019)
Advance Access publication 2019 February 20

doi:10.1093/mnras/stz508

Statistical analysis of the interplay between interstellar magnetic fields and filaments hosting *Planck* Galactic cold clumps

D. Alina ,[1,2] I. Ristorcelli,[2]★ L. Montier,[2] E. Abdikamalov,[1] M. Juvela,[3] K. Ferrière,[2] J.-Ph. Bernard[2] and E. R. Micelotta[3]

[1]*Department of Physics, School of Science and Technology, Nazarbayev University, Astana 010000, Kazakhstan*
[2]*IRAP, Université de Toulouse, CNRS, UPS, CNES, Toulouse, 31400, France*
[3]*Department of Physics, PO Box 64, University of Helsinki, FI-00014 Helsinki, Finland*

Accepted 2019 February 15. Received 2019 February 14; in original form 2017 December 26

ABSTRACT

We present a statistical study of the relative orientation in the plane of the sky between interstellar magnetic fields and filaments hosting cold clumps. For the first time, we consider both the density of the environment and the density contrast between the filaments and their environment. Moreover, we geometrically distinguish between the clumps and the remaining portions of the filaments. We infer the magnetic field orientations in the filaments and in their environment from the Stokes parameters,[1] assuming optically thin conditions. Thus, we analyse the relative orientations between filaments, embedded clumps, internal and background magnetic fields, depending on their environment and evolutionary stages. We recover the previously observed trend for filaments in low column density environments to be aligned parallel to the background magnetic field; however, we find that this trend is significant only for low-contrast filaments, whereas high-contrast filaments tend to be randomly orientated with respect to the background magnetic field. Filaments in high column density environments do not globally show any preferential orientation, although low-contrast filaments alone tend to have perpendicular relative orientation with respect to the background magnetic field. For a subsample of nearby filaments, for which volume densities can be derived, we find a clear transition in the relative orientation with increasing density, at $n_{\rm H} \sim 10^3$ cm^{-3}, changing from mostly parallel to mostly perpendicular in the off-clump portions of filaments and from even to bimodal in clumps. Our results confirm a strong interplay between interstellar magnetic fields and filaments during their formation and evolution.

Key words: polarization – methods: statistical – (ISM:) dust, extinction.

1 INTRODUCTION

First observed in extinction by interstellar dust particles (Schneider & Elmergreen 1979) and then in dust and CO emission (Abergel et al. 1994; Falgarone, Pety & Phillips 2001), filamentary structures in molecular clouds recently became central to many studies. There is growing evidence that filaments play a fundamental role in the onset of star formation for low- and high-mass stars. The unprecedented angular resolution and sensitivity of the *Herschel* (Pilbratt et al. 2010) maps of dust emission in the far-infrared (FIR) wavelength range made it possible to discover a network of filamentary structures ubiquitous in a wide range of environments of the ISM (Men'shchikov et al. 2010; Miville-Deschênes et al. 2010; Molinari et al. 2010; Motte et al. 2010; Juvela et al. 2012). Moreover, it was shown that prestellar cores and protostars form primarily in the densest and gravitationally bound filaments (André et al. 2010; Polychroni et al. 2013; Könyves et al. 2015). Investigating the origin and evolution of filaments is then crucial to better understand the early stages of star formation.

Magnetohydrodynamic (MHD) simulations show that a hierarchy of sheets and filaments can form as a result of shock-compression and shear flows in supersonic turbulence, at the same time as the collapse or fragmentation of gravitationally unstable structures (André et al. 2014; Li et al. 2014). Magnetic fields are believed to

★ E-mail: dana.alina@nu.edu.kz (DA); isabelle.ristorcelli@irap.omp.eu (IR)
[1]Based on observations obtained with Planck (http://www.esa.int/Planck), an ESA science mission with instruments and contributions directly funded by ESA Member States, NASA, and Canada.

play a key role in the formation of structures, but their interplay with turbulence and self-gravity still needs to be better understood at different spatial scales and evolutionary stages.

Observations of starlight polarization revealed a connection between the magnetic field geometry and the dense filamentary structures, finding predominantly perpendicular relative orientations between the mean field and the long axes of the filaments (Goodman et al. 1990; Pereyra & Magalhães 2004; Alves, Franco & Girart 2008; Franco, Alves & Girart 2010; Chapman et al. 2011). Studies of the magnetic field orientations derived from observations of starlight polarization are however limited to small regions and depend on the background star distribution. Alternatively, measurements of dust polarized thermal emission can also be used to trace the magnetic field geometry and allow us to probe denser media. This method was shown to be the most efficient way to reveal magnetic field structures in molecular clouds (Crutcher 2012). Such observations towards small bright regions of molecular clouds are performed from ground-based telescopes, and their high angular resolution is well suited to studies of prestellar cores (Dotson et al. 2000; Ward-Thompson & Kirk 2000; Matthews et al. 2009; Tang et al. 2009; Tassis et al. 2009; Pattle et al. 2017; Liu et al. 2018a). Massive dense cores with distances of a few kiloparsecs have been resolved using interferometric observations such as the Submillimeter Array (SMA), revealing the structure of the magnetic field at 0.1–0.01 pc scales (Koch et al. 2014; Zhang et al. 2014; Ching et al. 2017). The major axes of dense cores are found to be either parallel or perpendicular to the mean magnetic field at parsec scales, although at much smaller scale, typical of accretion discs, the relative orientation appears more random. These studies support the hypothesis that magnetic fields play an important role during the collapse and fragmentation of filaments and clumps, and the formation of dense cores. At smaller scales, kinematics arising from gravitational collapse would dominate over magnetic fields.

At the scales of filamentary structures, parallel relative orientation was observed between the mean magnetic field and either low-density sub-filaments (Sugitani et al. 2011) or the striation features revealed with Herschel in Taurus (Palmeirim et al. 2013), Musca (Cox et al. 2016), and in the high-Galactic latitude cloud L1642 (Malinen et al. 2016). A bimodal distribution of relative orientations was both observed in filamentary molecular clouds of the Gould Belt (Li et al. 2013) and predicted from MHD simulations (Nakamura & Li 2008; Soler et al. 2013; Li et al. 2016).

The *Planck*[2] satellite survey has recently provided the first all-sky map of dust polarized emission (Planck Collaboration XIX 2015a; Planck Collaboration 2018). With unprecedented sensitivity measurements at 353 GHz and a resolution of 5′, these data are uniquely suited to probe the dust polarized emission over a large range of column densities, at intermediate scales between molecular clouds and cold cores. Studying the relative orientation between the magnetic field and the column density structures at 15′ resolution and over most of the sky, Planck Collaboration XXXII (2016a) found that most of the elongated structures in the diffuse ISM have preferential parallel relative orientation with the magnetic field, while perpendicular structures appear in molecular clouds. In a detailed study of ten nearby molecular clouds of the Gould Belt, Planck Collaboration XXXV (2016c) showed that, as gas column density increases, the relative orientation changes from mostly parallel or having no preference to mostly perpendicular at high column densities. A similar trend was found in the Vela C molecular cloud observed with BLAST-POL at higher angular resolution (3′), with a sharp transition in $N_{\rm H}$ characterizing the change of relative orientation (Soler et al. 2013). Simulations show that such a change could be related to the degree of magnetization of the cloud, particularly when magnetic energy is in equipartition with turbulent energy (Hennebelle 2013; Chen, King & Li 2016; Soler & Hennebelle 2017). In a detailed study of three nearby filaments, Planck Collaboration XXXIII (2016b) showed that the mean magnetic fields inside the filaments are coherent along their lengths and do not have the same orientations as in the background. Moreover, the relative orientation between magnetic fields inside the filaments and in the background was shown to be different in the three studied cases. All these studies suggest that the magnetic field must play an important role in the assembly of interstellar matter and the formation of dense structures. Further statistical observations are required to characterize the range of scales and densities for which the magnetic field has a significant impact. To better understand the early stages of star formation, it is particularly important to study whether and how the properties of the ambient magnetic field are related to the filament evolution and prestellar core formation.

The *Planck* catalogue of Galactic cold clumps is built from the *Planck* full all-sky survey (Planck Collaboration XXVIII 2015c). The catalogue contains more than 13 000 cold sources distributed across the whole sky, from the Galactic plane to high latitudes, and are mainly situated in molecular clouds. The sources span a broad range in temperature, mean density, mass, and size. Because of the limited angular resolution, the most compact and nearby sources have a linear diameter of ∼0.1 pc, though at large distances, many sources have an intrinsic size of tens of parsec. As revealed by higher angular resolution observations performed with *Herschel* follow-up on a representative subsample of 350 *Planck* Galactic cold clump (PGCC) targets, these clumps are characterized by the presence of substructures. The clumps often contain colder and denser individual starless or prestellar cores and young protostellar objects still embedded in their colder surrounding cloud (Juvela et al. 2010, 2011; Planck Collaboration XXII 2011a; Juvela & Ysard 2012; Montillaud et al. 2015). As shown with a statistical analysis based on molecular dense tracers, most of the *Planck* clumps correspond to an early stage of star formation (Wu et al. 2012; Liu et al. 2015; Liu et al. 2016, 2017; Tatematsu et al. 2017). Furthermore, it was found that a substantial fraction of them are embedded in filamentary structures (Juvela et al. 2012).

In this work, our goal is to investigate the possible interplay between magnetic fields and filaments hosting PGCCs. Having selected a sample of these filaments surrounded by an ordered magnetic field, we perform a statistical analysis of the relative orientations in the plane of the sky between the filaments, their embedded clumps, and the magnetic fields inside and around the filaments.

This paper is organized as follows. In Section 2, we present the *Planck* data, the PGCC catalogue, and a description of the methods used for the filament detection and the separation of the polarization Stokes parameters (I, Q, U) between those intrinsic to the filaments and those of their surroundings. In Section 3, we present the properties of the filaments selected for this statistical study, and the subsamples built according either to the column densities of the filament environment or to the density contrast of the filaments. In Section 4, we describe the results obtained on the relative orientation between

[2] *Planck* (http://www.esa.int/Planck) is an ESA science mission with instruments and contributions directly funded by ESA Member States, NASA, and Canada.

the filamentary structures and the magnetic fields in the background and inside the filaments. We discuss the implications of these results in Section 5. Finally, Section 6 presents our conclusions and perspectives.

2 DATA AND METHODOLOGY

2.1 *Planck* data used and PGCC catalogue

In our analysis, we use the *Planck* 353 GHz full mission data, which is a part of the *Planck* Product 2015 release. In order to improve the signal-to-noise ratio (SNR), the data are smoothed from the nominal resolution of the maps (5′) to a resolution of 7′. The smoothing is performed using a convolution with a Gaussian kernel of 5′.

The *Planck* all-sky Galactic cold clump catalogue (Planck Collaboration XXVIII 2015b) contains 13 188 sources detected using a dedicated method (Montier et al. 2010; Planck Collaboration XXIII 2011b). The method consists of a colour-based detection of the excess emission in the cold residual maps after subtraction of the warm component traced by IRAS 100 μm observations. Clumps were fitted using elliptical Gaussian functions, and the catalogue contains the resulting semimajor and semiminor axes and the position angles of the ellipses. With the exception of some sources in the Large Magellanic Cloud and in the Small Magellanic Cloud, the catalogue excludes extragalactic sources (Planck Collaboration XXVIII 2015b) and contains nearby cores, clumps, and distant molecular clouds. This makes the catalogue particularly useful in studies related to the early stages of star formation. The *Planck* data are in HEALPix format, with a resolution parameter $N_{\rm side} = 2048$. We extract small 2 deg^2 maps centred on the positions of the clumps from the catalogue. Such maps are called minimaps hereafter. The pixel size is 1′. The Shannon–Nyquist criterion for sampling is thus satisfied. The slight oversampling does not affect our further analysis as it is based on histograms, and the uncertainties are estimated for independent pixels.

We select cold clumps from the PGCC catalogue using the following criteria:

(i) Clumps are within the Galactic latitude range $2^\circ \leq |b| \leq 60^\circ$ to avoid confusion along the line of sight (LOS) in the Galactic plane.

(ii) Clumps are detected with accurate flux density estimates in the *Planck* 545 and 857 GHz channels as well as in the IRIS 3 THz band. This corresponds to the PGCC catalogue flag `FLUX_QUALITY = 1`. We also include fainter sources: clumps for which there is no detection in the IRIS 3 THz band (flag `FLUX_QUALITY = 2`).

(iii) Clumps are detected with an SNR ≥ 8 in the three highest *Planck* frequency bands (857, 545, and 353 GHz).

(iv) Clumps have an average SNR on the polarized intensity ($P = \sqrt{Q^2 + U^2}$) SNR(P) ≥ 2. We use SNR(P) as it reflects the joint SNR of the Stokes parameters Q and U used in the estimation of the polarization angle (see equation 2). SNR(P) is estimated as P/σ_P, where $\sigma_P = \sqrt{\sigma_Q\,\sigma_U}$. Such an estimate of the uncertainty in the polarized intensity was discussed by Montier et al. (2015). SNR(P) is calculated in a disc of 10′ radius around the position of the clumps and in an annulus with inner and outer radii of 30 and 50′. We require $\langle P/\sigma_P \rangle \geq 2$ in both regions.

This yields a selection of 3743 clumps.

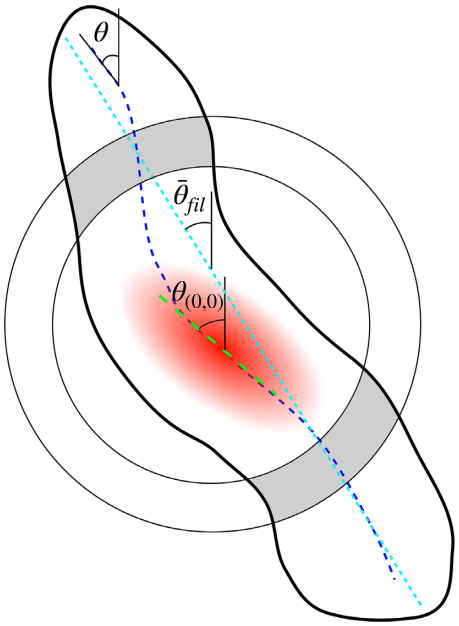

Figure 1. Schematics showing a filament with an embedded clump. The red area shows the clump ellipse. The green and light blue dashed lines show the SupRHT orientation at the centre of the clump (given by $\theta_{0,0}$) and the average orientation of the filament (given by $\bar{\theta}_{\rm fil}$), respectively. The angles $\Delta\bar{\theta}_{\rm up}$ and $\Delta\bar{\theta}_{\rm down}$, defined in the main text, are computed over the grey areas.

2.2 Filament detection method

Several methods exist to detect filamentary structures (Sousbie 2011; Soler et al. 2013; Planck Collaboration XI 2014). Among those, we opted for the SupRHT method, which is an improved version of the Rolling Hough Transform proposed by Clark, Peek & Putman (2014). It is a machine vision method that allows one to determine whether each pixel in an image belongs to a curve of a given shape. First, a map is smoothed using a two-dimensional 'top-hat' kernel. Secondly, a bitmask is built by subtracting the smoothed map from the original one and by thresholding the result at 0. Then, an input kernel of a given shape is applied. For each orientation of the input kernel, the method counts the number of pixels falling inside the kernel. The orientation angle θ in each pixel is defined as the average value of the SupRHT histogram after thresholding above a given value, set to 0.7 in our study. θ is counted positively in the direction from north to east and ranges between -90° and 90° (cf. Fig. 1). All the angles used in our analysis follow the same convention. The intensity $I_{\rm RHT}$ is defined as the sum of the histogram over all orientations. In the case where no kernel-like structure is detected at a given position, $I_{\rm RHT} = 0$. The main advantage of this method is that it is independent of the intensity of the structure with respect to the background intensity, as a top-hat filtering is performed before calculations. Another advantage is that it provides an estimate of the uncertainty in the angle (σ_θ). A disadvantage of the method is that it detects only structures with a shape similar to the input kernel.

We use the 353 GHz *Planck* minimaps, which we convolve with a bar kernel of length $k_{\rm s} = 31'$ and width $k_{\rm w} = 6'$ as an input to the method. The selection of the kernel's dimension is described in Appendix A.

We run the intensity minimaps centred on the pre-selected PGCCs through the SupRHT procedure. The raw SupRHT maps contain several overlapping filamentary structures. We isolate only the

filamentary structure associated with the PGCC in the centre of each minimap. Hereafter, we refer to such filamentary structures as filaments. We build a mask to isolate the clump ellipses defined by the semimajor and semiminor axes provided in the PGCC catalogue and the position angles $\theta_{0,0}$ in the centre of the clumps. We also build a mask to separate the area covered by clumps (which we refer to as the clump area) from the area covered by the rest of the filament (which we refer to as the filament area). The number of pixels in a filament ranges from ∼180 to ∼1200 with an average of ∼500. The number of pixels in a clump ranges from ∼50 to ∼500 with an average of ∼200, as shown in the histograms in Fig. C1.

For the clump in the centre of each minimap, we fit the histograms of the orientation angle, θ, inside the clump ellipse with a Gaussian function. We normalize the histograms to one and call them distribution functions (DFs). We derive the position of the peak, $\bar{\theta}_{\rm clump}$, and the standard deviation, $\sigma'_{\theta,\,\rm clump}$, of the DFs. The reason why we use a Gaussian fit is to obtain a good approximation of the average orientation angle over most pixels in the clump, which is not affected by the possible presence of pixels with a separate distribution. We define $\delta\bar{\theta}$ as the difference between $\bar{\theta}_{\rm clump}$ and the SupRHT orientation angle at the centre of the clump, $\theta_{0,0}$. The parameters $\sigma_{\theta,\,\rm clump}$ and $\delta\bar{\theta}$ allow us to ensure that the angle θ does not change much over the area of the clump ellipse, so that the pixels belong to the same filament.

We also calculate the average angles, $\bar{\theta}_{\rm up}$ and $\bar{\theta}_{\rm down}$, in the two regions of the filament contained between two circles centred on the clump centre and with radii equal to 1.5 and 2 times the clump's semimajor axis (see grey areas in Fig. 1). The absolute differences between these angles and $\theta_{0,0}$ are called $\Delta\bar{\theta}_{\rm up}$ and $\Delta\bar{\theta}_{\rm down}$. These parameters allow us to control the apparent length of the filaments and to put constraints on their curvature.

We apply the following criteria to the above parameters for the detection of linear filaments in our study:

(i) $I_{\rm RHT} \neq 0$ at the centre of each minimap;
(ii) $\sigma_\theta < 1^\circ$ at the centre of each minimap;
(iii) $\delta\bar{\theta} < 5^\circ$;
(iv) $\sigma'_{\theta,\rm clump} < 5^\circ$;
(v) $\Delta\bar{\theta}_{\rm down} < 15^\circ$ and $\Delta\bar{\theta}_{\rm up} < 15^\circ$;
(vi) if a filament contains several PGCCs and thus is detected several times, we retain only one minimap, but we consider the contributions of all the PGCCs in the filament.

This yields a pre-selection of 137 fields.

2.3 Coherence of the background polarization angle

The polarization signal towards a filament comes from the filament itself and both the background and foreground interstellar media. For convenience, we call the background and foreground contributions as the 'background'. We separate the background contribution from the observed signal using the following simple approach. We assume that the emission observed in the immediate surrounding of the filament is the same as the background emission at the location of the filament. Thus, the total signal in a pixel *i* towards the filament is

$$X_i = X_{\rm fil,i} + X_{\rm bkg,i}, \tag{1}$$

where $X_i = \{I_i,\ Q_i,\ U_i\}$ and the 'fil' and 'bkg' subscripts stand for 'filament' and 'background', respectively. Such an approach is only valid when the background is the same on both sides of a filament and for optically thin media which is the case at the *Planck* 353 GHz channel.

As our study is focused on the relative orientations between magnetic fields and matter structures, we seek filaments having uniform polarization angle in the background. In each minimap, we define two rectangular regions on both sides of the filament (e.g. in the left column of Fig. 2). The side rectangles are parallel to each other, and they are located at a distance equal to the width of the $I_{\rm RHT}$ filament at the position of the clump. They have the same lengths, defined by the ends of the $I_{\rm RHT}$ filament, and the same widths, set to 30′. Together, they constitute the background region of each minimap.

In a general case, the linear polarization angle is calculated using

$$\psi_i = 0.5\,\mathrm{atan}(-U_i,\,Q_i), \tag{2}$$

and the corresponding average plane-of-the-sky (POS) magnetic field orientation angle is obtained by rotation by 90°:

$$\phi_i = \psi_i + \frac{\pi}{2}. \tag{3}$$

In the side rectangles, we calculate the average Stokes Q and U parameters, $(\bar{Q},\ \bar{U})$, from which we derive the average POS magnetic field orientation angle, $\bar{\phi}$, using equationss (2) and (3). As the angles in the *Planck* data are counted positively in the direction from north to west, we bring them to the IAU convention adopted for all the angles in this study by taking the negative value of the Stokes U parameter. Globally, the Stokes linear polarization parameters have similar values on both sides of the detected filaments: at least 70 per cent of the filaments have Stokes parameters that do not differ by more than 50 per cent between both sides. However, in some cases, the difference between the two sides as well as the dispersion of the Stokes parameters on each side can be high. The dispersion of the Stokes parameters individually does not represent the angles dispersion. We calculate the standard deviation of the magnetic field orientation, σ_ϕ, in each region using circular statistics (Berens 2009). This allows us to characterize the coherence of the magnetic field in the background and to refine the minimaps selection for our analysis further in Section 3.1.

2.4 Separation of filament and background polarization parameters

In order to investigate the contributions from the filament and its background in the polarization angle maps, we separate their respective contributions when possible. For each pixel i in a filament, we estimate the average background Stokes polarization parameters, $Q_{{\rm bkg},i}$ and $U_{{\rm bkg},i}$, by averaging Q and U over appropriate cuts. If the uncertainty for the considered pixel is smaller than 10°, we use cuts passing through the side rectangles perpendicular to the filament at the pixel position. Otherwise, the cuts are perpendicular to the filament at the central pixel, that is, at the position of the corresponding PGCC. See Fig. 2 for examples of cuts. As a first approximation, in view of our assumption of optically thin medium (see Section 2.3), the Stokes polarization parameters of the filament at pixel i are obtained by subtracting the background contributions from the total signal:

$$\begin{aligned} Q_{{\rm fil},i} &= Q_i - Q_{{\rm bkg},i} \\ U_{{\rm fil},i} &= U_i - U_{{\rm bkg},i}. \end{aligned} \tag{4}$$

The background magnetic field angle $\phi_{{\rm bkg},i}$ and the magnetic field angle of the filament $\phi_{{\rm fil},i}$ are then calculated using equation (3) for each pixel in the filament. Fig. C2 shows the average Stokes linear polarization parameters as well as the standard deviations

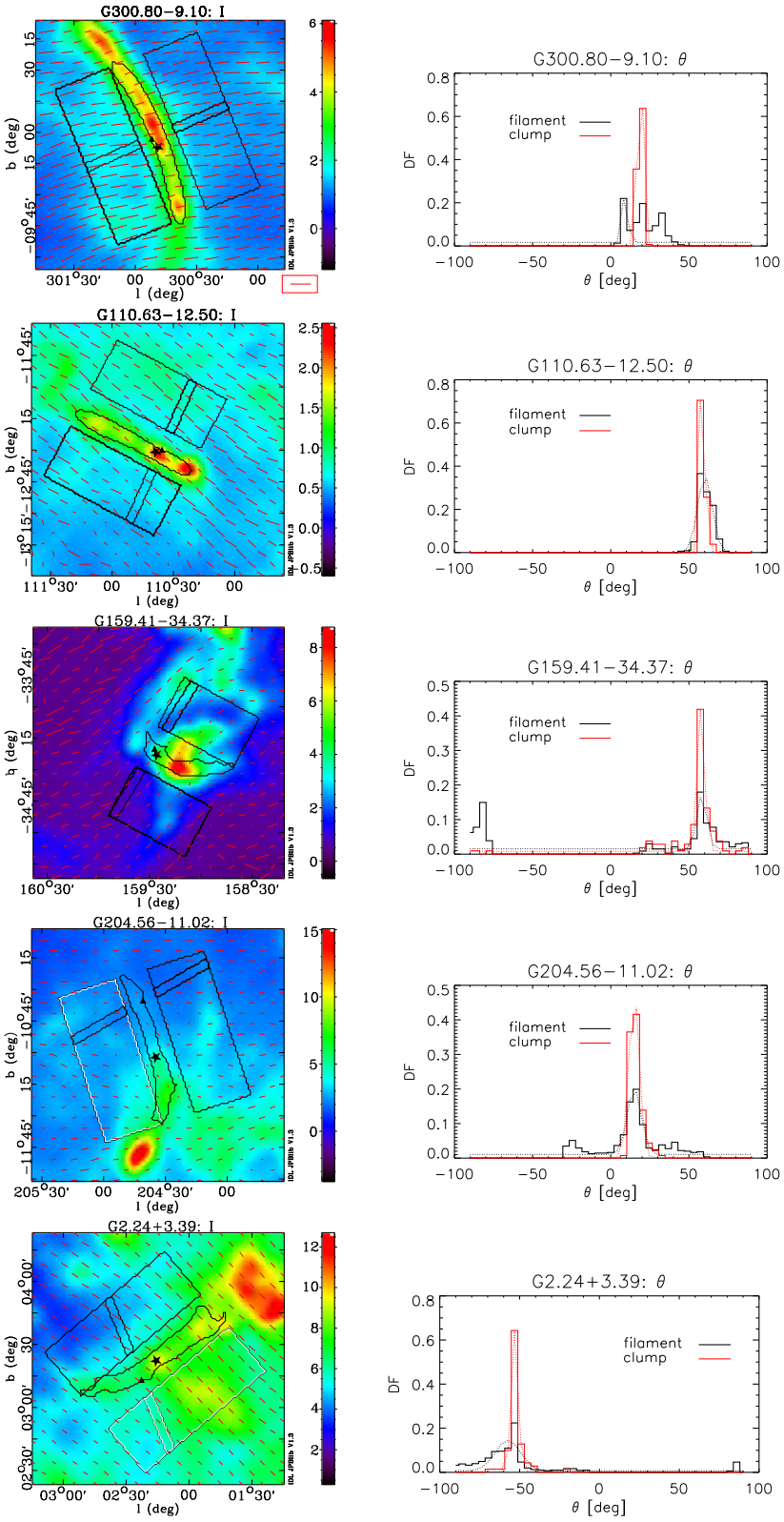

Figure 2. Examples illustrating the performed analysis. The left column shows the minimaps centred on the PGCC positions, indicated by a star. The colour scale shows the 353 GHz intensity in MJy sr^{-1}, while the red line segments represent the POS magnetic field orientation. In the first frame, the segment inside the red rectangle represents the reference length corresponding to 10 per cent polarization. The two black rectangles in each minimap delimit the regions used for determining the uniformity of the background magnetic field orientation (cf. Section 2.3). The contours between the rectangles show the extent of the detected $I_{\rm RHT}$ filament. Small black parallelograms delimit regions that correspond to the background area, for a pixel marked with the triangle, chosen randomly for illustration. The right column shows the normalized histograms of the filament orientation angles as well as the corresponding Gaussian fits, both for the entire filament (black line) and for the embedded clumps (red line).

for each filament before and after the estimated background level has been subtracted. On average, background subtraction does not critically change the linear polarization parameters. After background subtraction, the values of Q and U are changed by less than 20 per cent on average for 55 per cent of the filaments, and by less than 30 per cent for 70 per cent of them.

The above method is applied to the filament selection described further in Section 3.1. The selected filaments are embedded in an environment where the magnetic field orientation is uniform, so that our estimation of the linear background contribution is valid.

2.5 Column density

We determine the column density for each pixel using

$$N_{\rm H_2} = \frac{I_\nu}{\mu m_{\rm H}\, B_\nu(T)\, \kappa_\nu}, \quad (5)$$

where we adopt the dust opacity $\kappa_\nu = 0.1\,(\nu/1\,{\rm THz})^\beta\,{\rm cm^2 g^{-1}}$ (Beckwith et al. 1990), which is appropriate for the case of dense clouds at intermediate densities. μ is the mean molecular weight, which is equal to 2.8 amu in our analysis. The colour temperature T is estimated using the brightness emission in the *Planck* 857, 545, 353 GHz channels, and the IRIS 3 THz (100 μm) band. The maps were convolved to a 7 arcsec resolution and, for each pixel, the SED was fitted with $B_\nu(T)\nu^\beta$ using $\beta = 2$. This value is usually adopted for starless core studies and it is close to the mean value of β derived for *Planck* clumps (Planck Collaboration XXIII 2011b; Planck Collaboration XXVIII 2015c). I_ν is derived from the flux density at 857 GHz, the closest *Planck* band to the 1 THz reference of Beckwith et al. (1990), which minimizes the impact of assuming a fixed emissivity spectral index. This frequency also corresponds to the *Planck* HFI band where the SNR is the strongest.

3 FILAMENT SELECTION

3.1 The 'uniform background' selection

About 26 per cent of the pre-selected 137 filaments have the magnetic field angle dispersion larger than 20° in both background rectangular regions introduced in Section 2.3. Thus, most filaments are located in regions where the magnetic field orientation seen by *Planck* is coherent. To define the filaments that have a uniform magnetic field orientation in the background, we require that $\bar{\phi}$ does not change by more than 20° between both sides of the filament. This yields a selection of 90 objects distributed over the sky (cf. Fig. 3). The rest of our analysis is focused on this selection of filaments. Note that only 19 filaments out of the selected 90 fall into regions studied previously using *Planck* data (Planck Collaboration XXXV 2016c; Planck Collaboration XXXIII 2016b). Thus, most of the selected minimaps have not been the subjects of previous statistical studies on the relative orientation of magnetic fields and matter structures in the *Planck* data.

3.2 Characteristics of the selected filaments

Temperatures are reported in the PGCC catalogue for 80 per cent of the selection and span between 9 K and 19 K with a mean value of 13.7 K. Distance estimates are provided for about 45 per cent of the PGCCs and are mostly lower than 1 kpc. The corresponding histogram, presented in Fig. C3, shows a main peak at ∼0.2 kpc, and a second peak at ∼0.4 kpc. Masses are determined for 38 clumps. The masses of the 5 most distant clumps exceed 100 $M_\odot$

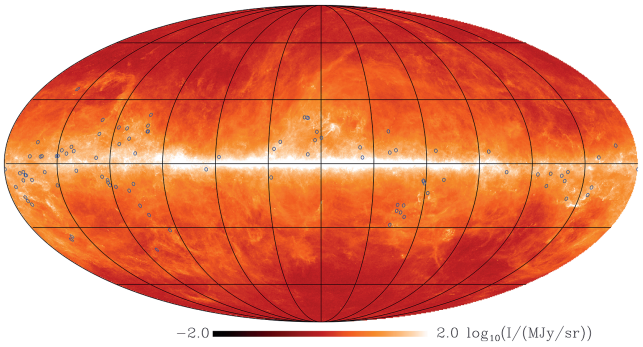

Figure 3. Positions of the 90 PGCCs selected for this study. The background map shows the intensity map at the *Planck* at 857 GHz in logarithmic scale.

and approach the masses of molecular clouds. However, 21 clumps, which represent 23 per cent of the selection, have their masses found to be smaller than 5 $M_\odot$ with a mean value of 2.02 $M_\odot$. The average gas column densities calculated according to equation (5) range from $2.9 \times 10^{20}\,{\rm cm^{-2}}$ to $2.5 \times 10^{22}\,{\rm cm^{-2}}$ with a mean value of $3 \times 10^{21}\,{\rm cm^{-2}}$.

We estimate the average sizes of the clumps as

$$C = 2\sqrt{ab}, \quad (6)$$

where a and b are the semimajor and semiminor axes. The average sizes range from 10 to 17′ with an average of 13′. The corresponding histogram is presented in Fig. C4. The lengths of the selected filaments, which are estimated as the sum of the two line segments connecting the centre of the clump to the ends of the filament, range from 34 to 104′ with an average value of 66′. The widths of the filaments at the centre of the clumps range from 4 to 20′ with an average value of 8′. The ratio of the longest to shortest axes of the filaments varies from 3 to 18 with an average of 9. We emphasize that the lengths and widths given here are not the physical dimensions, but just detection dimensions. These parameters depend on the detection method and the kernel size used in the SupRHT method.

A conservative estimate of the dispersion of the magnetic field angle in the filaments, calculated using circular statistics, ranges from 6° to 73° with a mean value of 40°.

3.3 Column density subsamples

Following the observation that the preferential orientation of matter in filaments with respect to the background magnetic field changes with gas column density (Planck Collaboration XXXV 2015d), we divide our selection of filaments into two subsamples according to the column density of their environment. We separate these two using a threshold column density equal to the median background column density of $1.2 \times 10^{21}\,{\rm cm^{-2}}$. The corresponding subsamples are called $N_{\rm H,bkg}^{\rm high}$ and $N_{\rm H,bkg}^{\rm low}$.

We also distinguish between filaments that are more or less contrasted with respect to their environment by calculating the column density contrast:

$$\Delta N_{\rm H} = \bar{N}_{\rm H} - \bar{N}_{\rm H,\,bkg}, \quad (7)$$

where $\bar{N}_{\rm H}$ is the average column density over the filament area and $\bar{N}_{\rm H,\,bkg}$ is the average column density in the background area. We denote $\Delta N_{\rm H}^{\rm low}$ and $\Delta N_{\rm H}^{\rm high}$ the subsamples of filaments that have differential column densities lower and higher than the median $\Delta N_{\rm H}$ of $4 \times 10^{20}\,{\rm cm^{-2}}$.

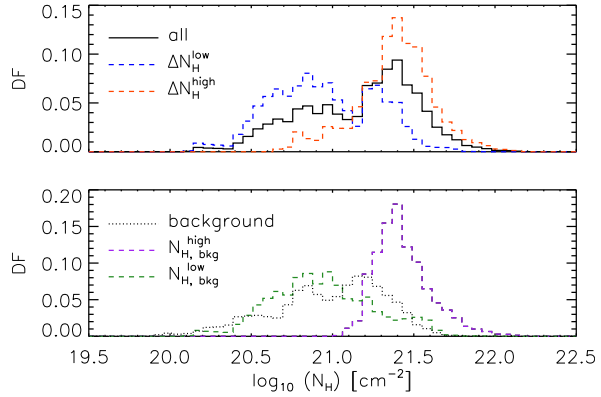

Figure 4. DFs of the column density in the pixels of the detected filaments. In the upper panel, the black solid line represents all filaments, the blue and red dashed lines represent the low and high differential column density subsamples. In the lower panel, the grey dotted line represents the background regions, the green and purple lines show the low and high background column densities subsamples.

Table 1. Number of filaments in background and differential column density subsamples (cf. Section 3.3). The threshold column densities between subsamples are $N_{\rm H,\,bkg} = 1.2 \times 10^{21}$ cm^{-2} and $\Delta N_{\rm H} = 4 \times 10^{20}$ cm^{-2}. In parentheses, we report the number of filaments with known distances in each of the subsamples.

	$N_{\rm H,bkg}^{\rm low}$	$N_{\rm H,bkg}^{\rm high}$	Total
$\Delta N_{\rm H}^{\rm low}$	30	15	45 (17)
$\Delta N_{\rm H}^{\rm high}$	15	30	45 (9)
Total	45 (9)	45 (17)	

The histograms of the column density normalized to one for the various subsamples are shown in Fig. 4. The number of detected filaments in each subsample is reported in Table 1. The distribution of the number of pixels in the filament and clump areas in the different subsamples are roughly the same and follow the general distribution shown in Fig. C1. We emphasize that the PGCCs chosen for this study are outside of the Galactic plane and the observed column densities are more probably due to local structures rather than averaging along long LOS. We observe in Fig. 4 that with our selection we probe environments with different column densities, shown by the grey dotted line in the lower panel. We also note that filaments embedded in high column density environments tend to have higher column densities. The same behaviour was observed in *Herschel* data at smaller scales (Rivera-Ingraham et al. 2017), where dense filaments tend to be embedded in dense environments.

4 RESULTS

Above, we obtained the orientation angles of matter in all the pixels of our filaments (θ_i), the average orientation angles of matter in the filament and clump areas ($\bar{\theta}_{\rm fil}$ and $\bar{\theta}_{\rm clump}$), and the magnetic field angles in all the pixels of the filaments and their background ($\phi_{{\rm fil},i}$ and $\phi_{{\rm bkg},i}$). We separated the filaments into subsamples depending on the column density of the background and on the column density contrast.

In what follows, we investigate the relative orientation between matter and magnetic fields depending on the filament characteristics such as the background column density and the column density contrast. We omit the subscript i to simplify the expressions.

4.1 Relative orientation between filaments and embedded clumps

We calculate the absolute difference between the average orientation angles within the filament and clump areas $|\bar{\theta}_{\rm fil} - \bar{\theta}_{\rm clump}|$ (cf. Section 2.2). For this purpose, only elongated clumps with ellipticities larger than 1.5 are used. As an orientation angle corresponds to two possible directions, we consider only the smallest angle between the two line segments, which is in the range from 0° to 90°. Most (∼98 per cent) of the clumps have their major axes aligned with their hosting filament within 20°. The same is observed when clumps with ellipticities smaller than 1.5 are included in the analysis.

In order to check that this result is independent of the filament detection method, we compare the average clump position angles $\bar{\theta}_{\rm clump}$ given by SupRHT to the position angles $\theta_{\rm cat}$ provided in the PGCC catalogue, which is based on the cold residual maps. In the latter case, 90 per cent of the clumps are on average aligned with the filament within 20°. Both methods agree on the position angle of the clumps within 20° for more than 70 per cent of the selection. If we consider clumps with all ellipticities, this fraction goes down to 62 per cent. We note that these differences may also come from uncertainties in the detection method used to build the PGCC catalogue.

4.2 Relative orientation between filaments and the background magnetic field

In this section, we investigate the statistics of the relative orientation between filaments and the background magnetic field. To this end, we calculate the absolute difference between the average background magnetic field angle and the position angle for each pixel ($|\phi_{\rm bkg} - \theta|$). This quantity is also defined in the range from 0° to 90°. We do not calculate this quantity per filament because the size of our sample is not sufficient for significant statistics.

We show in the upper panel of Fig. 5 the DFs over pixels in the filament area belonging to the low and high background column density subsamples. In low-density environments, the number of pixels decreases by a factor of 2 when increasing the value of $|\phi_{\rm bkg} - \theta|$, that is from parallel to perpendicular relative orientation, whereas in dense environments filaments have no preferential relative orientation with respect to the background magnetic field. In the lower panel of Fig. 5, featuring the same analysis for the clump areas, we observe not only strong peaks at 0° but also a significant distribution at large $|\phi_{\rm bkg} - \theta|$. The two-clump DFs look similar but the $N_{\rm H,bkg}^{\rm high}$ subsample has a slightly larger probability for either parallel and perpendicular relative orientations.

We carry out a non-parametric Mann–Whitney *U*-test (called *U*-test hereafter) in order to quantify the difference between the two pairs of distributions. The *U*-test probability for the DFs of the filament areas is 10^{-7}, indicating that the distributions of $|\phi_{\rm bkg} - \theta|$ in the low and high column density background subsamples are statistically different. The *U*-test probability for the DFs of clump areas is 0.21 that confirms that the distributions of $|\phi_{\rm bkg} - \theta|$ in the low and high background column density are similar. The *U*-test on the DFs of the filament areas versus clump areas yields 0 probability of similarity between both subsamples. The summary of the trends observed in the above DFs is provided in Table 2.

For each subsample, we further separate the contributions from the filaments depending on their column density contrast with respect to their environment. Fig. 6 shows the DFs over the filament and clump areas in the low background column density subsample ($N_{\rm H,bkg}^{\rm low}$). We observe that, in the filament areas (upper panel of

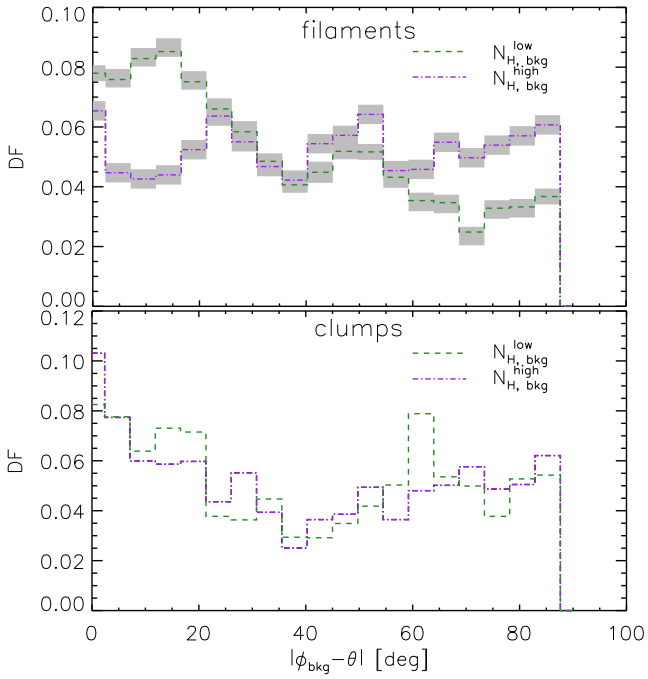

Figure 5. DFs of the absolute difference between the orientations of the background magnetic field and the matter structures. The green dashed and purple dot–dashed lines are for low and high background column density subsamples, respectively. Upper panel: filament areas; lower panel: clump areas. For illustration purpose, uncertainties are reported in grey shaded areas in the upper panel.

Fig. 6), there is much less parallel relative orientation in the high column density contrast subsample than in the low column density contrast subsample. The corresponding DFs over the clump areas in the lower panel of Fig. 6 show that, again, there is a tendency for parallel relative orientation in the low-contrast filaments. In the DF of high-contrast filaments, there is a peak around 60°. The peak is not conclusive, as it cannot be interpreted as perpendicular relative orientation. This could arise from projection effect of the perpendicular relative orientation or be a trace of the oblique orientations of the clumps in 3D due to the rotation of the clumps during the filament evolution. In an attempt to investigate the origin of these two peaks, we separate the clumps inside the low background column density subsample into two parts depending on their average column density. The corresponding histograms are shown in Fig. C5. We recover the similar kind of figure as shown in the lower panel of Fig. 6 for $N_{\rm H}$ equal around 2×10^{21} cm^{-2}. There is a clear dichotomy depending on the column density: high column density clumps show a preferential perpendicular relative orientation, whereas the lower column density clumps show parallel relative orientation with respect to the background magnetic field.

Fig. 7 shows the DFs of $|\phi_{\rm bkg} - \theta|$ over the filament (upper panel) and clump (lower panel) areas in the low background column density subsamples. For the filament areas, there is a tendency for perpendicular relative orientation in the $\Delta N_{\rm H}^{\rm low}$ subsample, whereas in the $\Delta N_{\rm H}^{\rm high}$ subsample, there is a preferential parallel relative orientation with respect to the background magnetic field (the upper panel of Fig. 7). For the clump areas, the DF of the $\Delta N_{\rm H}^{\rm low}$ subsample shows a uniform distribution of $|\phi_{\rm bkg} - \theta|$, while the clumps inside the $\Delta N_{\rm H}^{\rm high}$ filaments tend to be aligned parallel to the background magnetic field. The *U*-test probability for the four pairs of distributions are below 10^{-7}, which means that the DFs of these column density subsamples are statistically different.

The uncertainties of the DFs are estimated using the bootstrap technique consisting of random sampling with replacement (Efron & Tibshirani 1993). The details on the uncertainties calculation using independent pixels are described in Appendix B. For illustration purpose, uncertainties are reported for some of the DFs. The rest of the uncertainties are of similar magnitude.

4.3 Relative orientation between filaments and their internal magnetic fields

In order to analyse whether there is any coherence between the filaments orientation and the magnetic field orientation inside filaments, we calculate the absolute difference between the respective angles in each pixel (θ and $\phi_{\rm fil}$). Fig. 8 shows the DFs over the pixels in both the filament and clump areas. The DFs show strong peaks at 0° regardless of the column density contrast (Fig. 8). However, in the filament areas (upper panel of Fig. 8), the distribution is flatter for the high column density contrast subsample than for the low-contrast subsample. Clumps inside these filaments (lower panel of Fig. 8) also tend to be less parallel to the filament magnetic field. In addition, the corresponding DF shows a strong peak near perpendicular relative orientation. Clumps inside the low-contrast filaments globally show a preferential parallel relative orientation with respect to the filament magnetic field. The *U*-test probability for the two pairs of distributions are equal to 0, which means that the DFs are statistically different. The summary of the tendencies observed in the above DFs is provided in Table 3.

To further investigate the bimodal distribution observed for clumps counterpart in the $\Delta N_{\rm H}^{\rm high}$ subsample, we separate the contributions from the low and high background column density subsamples, although the statistics are low when dividing the subsamples. The corresponding histograms are shown in Fig. 9. The peak near perpendicular relative orientation seen in the lower panel of Fig. 8 also appears in the low column density subsample, but not in the high column density subsample. This could arise from the component separation method. Indeed, subtracting a high background level strongly reduces the measured polarization degree and, therefore, makes the magnetic field angle estimation uncertain.

4.4 Relative orientation between magnetic fields inside the filaments and in the background

We calculate the difference between magnetic field angles inside the filament areas and in the background using the Stokes parameters of both regions (Planck Collaboration XIX 2015a) and is equal to the difference between the respective polarization angles:

$$\psi_{\rm fil} - \psi_{\rm bkg} = \frac{\mathrm{atan}(Q_{\rm fil}U_{\rm bkg} - U_{\rm fil}Q_{\rm bkg}, Q_{\rm fil}Q_{\rm bkg} + U_{\rm fil}U_{\rm bkg})}{2}. \quad (8)$$

Fig. 10 shows the corresponding DFs for the column density contrast subsamples. For the low-contrast filaments, the relative orientation is mostly parallel. For the high-contrast filaments, there is a slight tendency for parallel relative orientation with globally no preferential relative orientation.

Fig. C6 shows the DFs of the difference between the magnetic fields in the filament and in the background for the background column density subsamples. Even though the fields are mostly parallel in both, the DF of the $N_{\rm H,bkg}^{\rm high}$ subsample is flatter than the DF of the $N_{\rm H,bkg}^{\rm low}$ subsample.

Table 2. Summary of the results shown in Figs 5–7. The observed tendencies of the relative orientation between the filaments and the background magnetic field. $N_{\rm H,bkg}$ stands for the filaments in the environments with average column densities lower or higher than 1.2×10^{21} cm^{-2}. $\Delta N_{\rm H}^{\rm low}$ and $\Delta N_{\rm H}^{\rm high}$ stands for the filaments that are contrasted with respect to their environment by more or less than 4×10^{20} cm^{-2}.

	$N_{\rm H,bkg}$	Both $\Delta N_{\rm H}$	$\Delta N_{\rm H}^{\rm low}$	$\Delta N_{\rm H}^{\rm high}$
Filament areas	Low	Mostly ∥	Mostly ∥	No tendency
	High	No tendency	Mostly ⊥	Slightly ∥
Clump areas	Low	∥ and ⊥	Mostly ∥	Peak at $\simeq 60^\circ$
	High	∥ and ⊥	No tendency	Mostly ∥

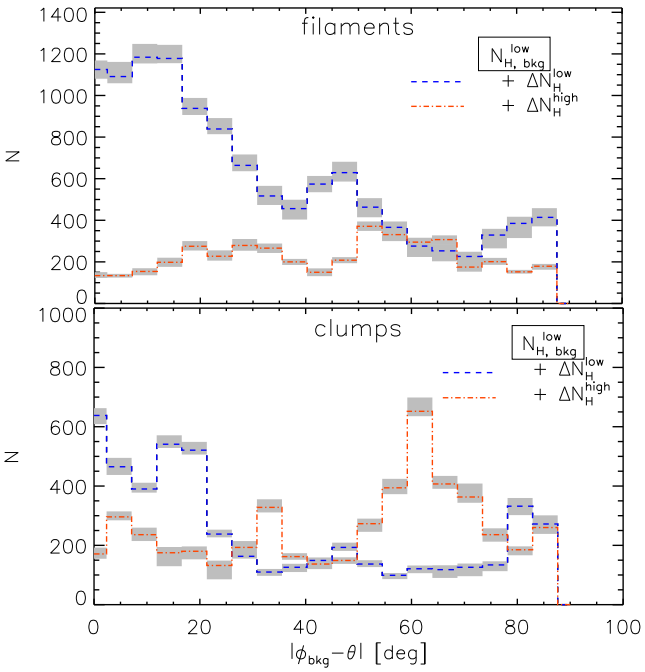

Figure 6. Histograms of the absolute difference between the orientation of the filamentary structures and the background magnetic field orientation over the pixels in the filaments only (upper panel) and in the clumps only (lower panel) for the low background column density subsample. Blue and orange dashed lines correspond to the contributions of the low and high-contrast filaments to each subsample. The uncertainties are shown in grey shaded areas.

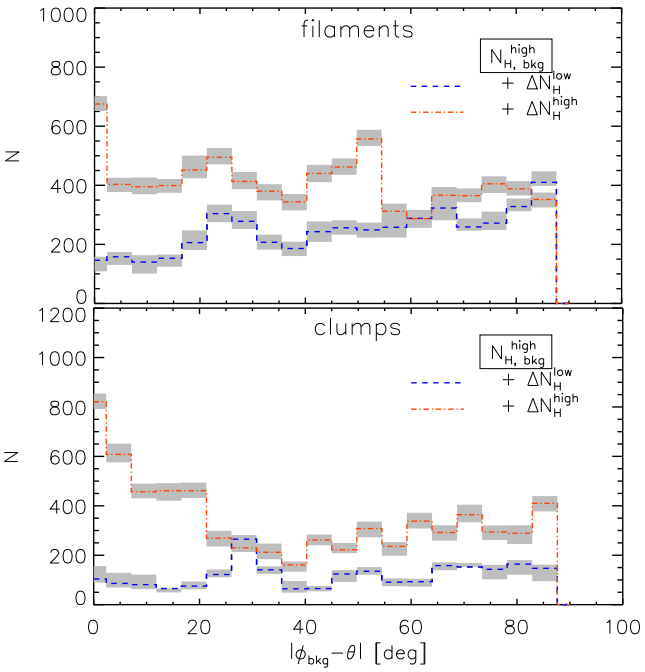

Figure 7. Histograms of the absolute difference between the orientation of the filamentary structures and the background magnetic field orientation over the pixels in the filament areas (upper panel) and in the clump areas (lower panel) for the high background column density subsample. Blue dashed and orange dot–dashed lines correspond to the contributions of the low and high-contrast filaments to each subsample. The uncertainties are shown in grey shaded areas.

Planck Collaboration XXXIII (2016b) estimated the average difference between the magnetic field orientation in the filaments and in their background for three filaments: Musca, Taurus L1506, and B211. They used polynomial fits to the Q and U parameters after subtraction of the background contribution. The first two filaments (Musca and L1506) are included in our final selection. For these two clouds, we obtain average values of the difference between magnetic fields in the filament and in the background of $8.6^\circ \pm 2^\circ$ and $55^\circ \pm 2^\circ$, which are comparable to, respectively, 10.6° and 57.1° obtained by Planck Collaboration XXXIII (2016b).

4.5 Nearby filaments

We calculate rough estimates of the mean gas volume densities for the clumps and filaments with known distances d in nearby molecular clouds. In our selection, there are 26 PGCCs situated within 500 pc from the Sun. The clumps can be approximated by spheres of radius $R = d\,C$ and the mean gas volume density of a clump is given by

$$\langle n_{\rm H} \rangle_{\rm clump} = \frac{3\,\langle N_{\rm H} \rangle_{\rm clump}}{4R}. \quad (9)$$

Assuming that the filament depth is equal to the filament width, the mean gas volume density of a filament is given by

$$\langle n_{\rm H} \rangle_{\rm fil} = \frac{\langle N_{\rm H} \rangle_{\rm fil}}{2dw}, \quad (10)$$

where w is the filament angular width. This yields only a rough estimate for the volume densities of the filaments since the width taken here is the detection width that underestimates the filament width as seen in the intensity maps. Also, the beam dilution prevents the detection of the densest regions. The average POS diameters of the clumps (widths of the filaments) in parsecs varies from 0.4(0.9)

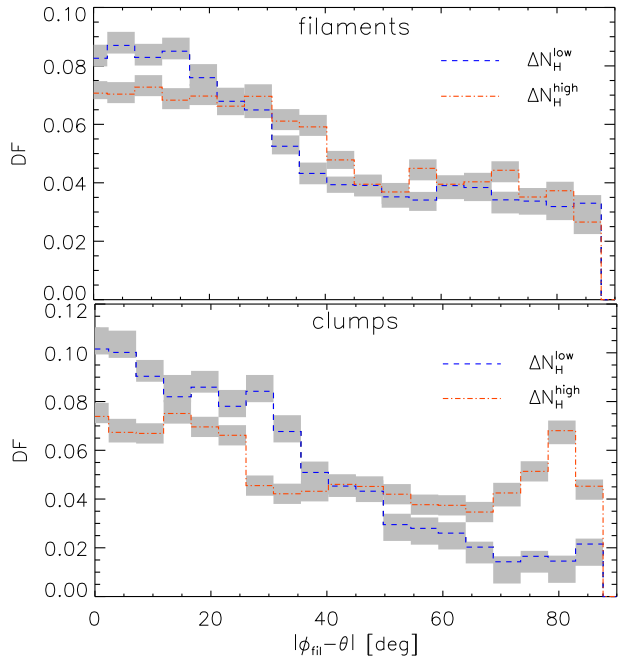

Figure 8. DFs of the absolute difference between the orientation of the filaments and the magnetic field angle in the filaments. In each panel, the blue and orange dashed lines represent the DFs over the pixels in the low- and high-density contrast subsamples. Upper panel: filament areas; lower panel: clump areas. The uncertainties are shown as grey shaded areas.

Table 3. Summary of the results shown in Fig. 8. The observed tendencies of the relative orientation between the filaments and the magnetic field in the filaments. ΔN_H stands for the column density contrast which is lower or higher than 4×10^{20} cm^{-2}.

ΔN_H	Filaments	Clumps
Low	Mostly ∥	Mostly ∥
High	Mostly ∥	∥ and ⊥

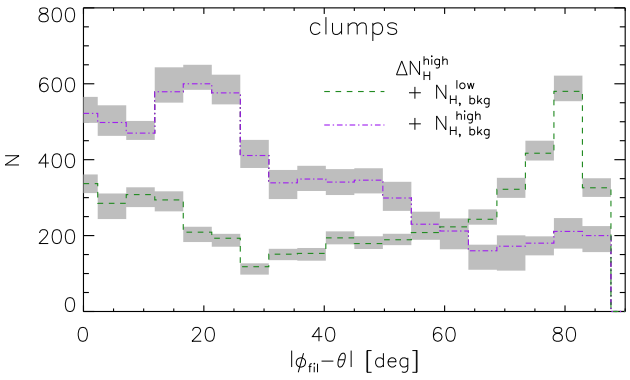

Figure 9. Histograms of the absolute difference between the orientation of the filamentary structures and the magnetic field direction in the filaments of the high column density contrast subsample in the clump areas. Green and purple dashed lines correspond to the structures embedded into a low- and high-density environment, respectively. The uncertainties are shown in grey shaded areas.

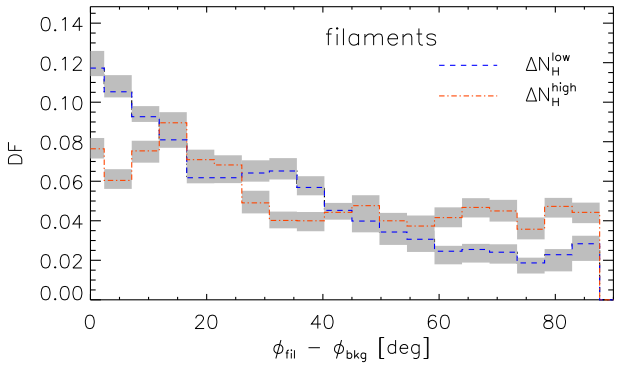

Figure 10. DF of the average difference between the magnetic field angles in the filaments and in the background. The blue and red lines show the DFs for the low- and high-contrast filament subsamples, respectively. The uncertainties are shown as grey shaded areas.

to 2.1(4.9) with an average of 0.9(2.2). The respective histograms are shown in Fig. C7. The majority (25 out of 26) of the clumps have an average radius smaller than 1 pc. The histograms of the mean volume densities of the clumps and associated filaments are shown in Fig. C8. n_H ranges between 400 and 1.2×10^4 cm^{-3} with an average value of 2500 cm^{-3} for the clumps, and between 150 and 4000 cm^{-3} with an average value of 1000 cm^{-3} for the filaments. Among the 26 filaments, we identify those belonging to the N_H subsamples, and the resulting numbers are reported in Table 1.

We test the results shown previously on the PGCCs with known distances. Globally, we observe the same behaviour as for the whole selection with few additional features detailed below. In the clumps, the contrast between the two column density contrast subsamples is slightly enhanced at low angles with the clumps associated with the filaments in high column density environment being more parallel with the background magnetic field. Inside the filament areas, the magnetic field and matter show mostly no preferential relative orientation in the ΔN_H^{high} subsample. Inside the clumps, perpendicular alignment is now also observed in the ΔN_H^{low} subsample.

Thresholding in $N_{H,bkg}$ and ΔN_H does not yield a threshold in n_H: there is a mix of low and high n_H filaments and clumps in the four subsamples considered previously. However, the average, minimal, and maximal values are shifted towards lower or larger values according to the N_H subsamples. For example, the average n_H value is equal to ∼700 cm^{-3} in the ΔN_H^{low} and ∼1500 cm^{-3} in the ΔN_H^{high} subsamples. We find a preferential perpendicular alignment in the filament areas located in filaments (6 out of 26) with $\langle n_H \rangle_{fil} > 1200$ cm^{-3}, while in those with lower gas volume densities there is few perpendicular alignment. The corresponding DF is shown in Fig. 11. In the clumps, we do not observe any particular difference compared to the results shown in Fig. 5.

We perform the same analysis to study the relative orientation between the orientation of matter in the filament areas and magnetic field inside the filaments. As it could be expected from Fig. 8, there is a rather parallel relative orientation of matter in the filaments areas with respect to inner magnetic field. A difference in the DFs is observed when considering the clumps areas. The behaviour is found to change around $\langle n_H \rangle_{clump} = 2900$ cm^{-3} and the corresponding DF is shown in Fig. 12. Above this density value, which applies for 7 clumps out of 26, the perpendicular counterpart of the relative orientation between the inner magnetic field and the clumps is important. However, below this value the DF is flat and

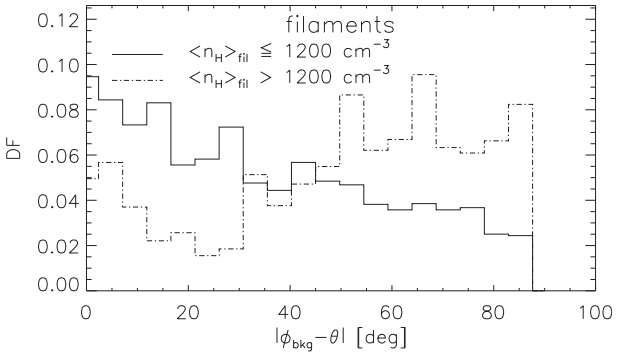

Figure 11. The DFs of the relative orientation between the background magnetic field and filaments only for the PGCC with known distances.

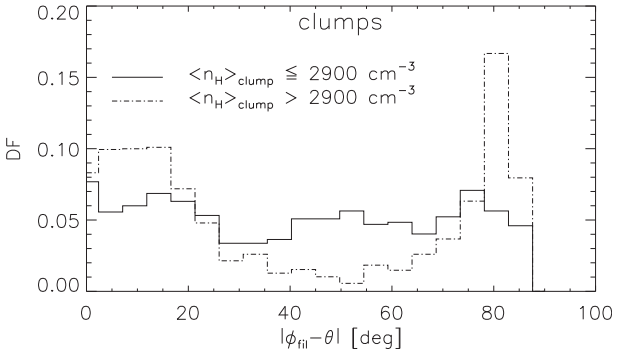

Figure 12. The DFs of the relative orientation between the inner magnetic field and clumps only for the PGCC with known distances.

is not as conclusive as in the case of the column density contrast subsamples.

5 DISCUSSION

We have presented a statistical analysis of the relative orientations in the POS between interstellar magnetic fields and filaments that were detected in the 353 GHz *Planck* data and found to host *Planck* cold clumps. We selected 90 such filaments all over the sky, excluding the Galactic plane, and retaining only filaments embedded in an environment with uniform magnetic field orientation. The selected filaments span a range of background gas column density N_H from 1.2×10^{20} cm^{-2} to 3.8×10^{21} cm^{-2} (averaged values at an angular resolution of 7′).

The two main novelties of our study are the following. First, we separated the respective contributions of the filaments and their background, assuming optically thin emission. This separation enabled us to study the effects of the environment and of the evolutionary stages of the filaments through the background column density and column density contrast, respectively. Secondly, in each filament, we drew a distinction between the area covered by clumps (clump area) and the remaining area of the filament (filament), in order to investigate possible different links between these structures relatively to the magnetic fields.

An advantage of our approach is in its applicability to large samples. Having estimated the background contribution at some POS distance from the filament, we could have missed the contribution of the immediate surroundings. However, the comparison with the results from detailed modelling of three individual filaments (Planck Collaboration XXXIII 2016b) shows that this assumption is valid and introduces only a few degrees bias, which is negligible for the qualitative conclusions of our analysis. In addition, we did not account for projection effects. As pointed out by Planck Collaboration XXXII (2016a), projection effects can produce a broadening of the DFs at parallel relative orientation, whereas an observed perpendicular trend indicates a true perpendicular relative orientation in 3D.

The process of filament formation is generally governed by the interplay between turbulence, self-gravity, and magnetic fields. A statistical analysis of the relative orientations between filaments and magnetic fields can bring new insights into the impact of magnetic fields. Our large sample of filaments within different Galactic environments offers a distribution of viewing angle that may be assumed mainly random.

Below, we discuss the results presented in this work and compare them to previous studies.

(i) At the filament scale:

The *Planck* all-sky survey offers a unique opportunity for statistical studies of the magnetic field and density structures down to the scale of filaments and clumps. The previous studies of the relative orientation between magnetic fields and filamentary structures have been performed at large scales, from intermediate and high Galactic latitudes diffuse ISM (Planck Collaboration XXXII 2016a) to nearby molecular clouds of the Gould Belt (Planck Collaboration XXXV 2016c).

The observed change of relative orientation with increasing N_H, from mostly parallel or having no preferred orientation to mostly perpendicular, has emphasized the significant role played by the magnetic field in shaping the structures in the diffuse ISM and molecular clouds. These observations were found to be in agreement with the predictions from numerical simulations of sub- or trans-Alfvénic MHD turbulence, where the magnetic field imposes an asymmetry in the formation of condensations from the diffuse ISM (Li et al. 2014). In this scenario, as discussed by Soler & Hennebelle (2017), low-density filaments could be produced by velocity shear induced by turbulence, stretching matter and magnetic field lines simultaneously, and resulting in parallel relative orientations between both.

More generally, in simulations with strong magnetic fields, the gas tends to be channelled along the field lines, and therefore converging flows driven by either large scale turbulence or self-gravity naturally produce dense filaments perpendicular to the magnetic field lines (Nakamura & Li 2008; Price & Bate 2008). These converging flows could also explain the presence of less dense filaments (such as striations) along the magnetic field lines (Stone, Ostriker & Gammie 1998; Li et al. 2016). Magnetic fields lines may also be orientated along compressed gas regions at the fronts of the shocks between expanding bubbles that are supernova remnants or expanding H II regions (Inutsuka et al. 2015).

The contraction in the direction of the field lines that results in the formation of denser filaments and/or cores with their main axes perpendicular to the magnetic field direction was already suggested in the observational studies from Palmeirim et al. (2013) in Taurus, Matthews (2013) in Lupus regions, or by Cox et al. (2016) in Musca and Malinen et al. (2016) in L1642.

Our results cannot be directly compared to those from Planck Collaboration XXXV (2016c), where the derived polarization angles at the location of the filaments include the background contribution and the clumps counterparts that can both have an impact in the histograms of relative orientation as shown in our study. Moreover, the alignment parameter used in Planck Collaboration XXXV

(2016c) is sampled within large angular range (20°) that fosters either parallel or perpendicular relative orientations and cannot be directly compared to our analysis based on the trends observed in the histograms.

However, we confirm the commonly observed parallel relative orientation for the filaments located in low-density environments, though with further interesting results. By distinguishing subsamples according not only to the environment density but also to the filament density contrast, we observe different trends. In low-density environments, although there is a clear parallel alignment for low-contrast filaments (upper panel of Fig. 6), the ones with high contrast do not show any preferential alignment with respect to the background magnetic field. These results suggest that even if the low-density regions are mostly dominated by turbulence and magnetic fields, self-gravity must play a significant role for higher density structures, resulting in an almost flat histogram of the relative orientations with the magnetic fields.

In high-density regions, the orientation of the high-contrast filaments do not show any dependence on the magnetic field orientation (the upper panel of Fig. 7). This may indicate that gravity is also the dominant factor in this case. In fact, these structures with high-density contrast can also be directly interpreted as the signature of regions where self-gravity dominates. On the contrary, the low-contrast filaments exhibit a preferential perpendicular relative orientation that could be explained by a more important role of the magnetic field at this stage of evolution.

The limited angular resolution of the *Planck* data does not allow to probe the inner structure of the filament magnetic field, but still enables to estimate its mean orientation, as shown in (Planck Collaboration XXXIII 2016b). We observe that the mean field is mainly parallel to the filament in both column density contrast subsamples, but shows slightly different trends. This may indicate that the low-contrast filaments are formed mostly by turbulent motions or large scale dynamics (like global collapse) that tend to compress simultaneously the matter and the magnetic field. The flatter distribution for the high-contrast filaments suggests that the magnetic field is altered during the gravitational contraction.

(ii) On the transition in N_H:

The selection of the two background column density subsamples corresponds to a division at the median value of our initial sample $N_{\rm H,bkg} = 1.2 \times 10^{21}$ cm^{-2}. It can, however, be compared to the threshold value in Planck Collaboration XXXV (2016c) who derives $N_{\rm H} \sim 5 \times 21$ cm^{-2} that gives $N_{\rm H} \sim 2 \times 21$ cm^{-2} when using the same opacity κ value (there is a factor of ∼2.5 between the dust models opacity values adopted for the diffuse and the dense medium). It is also close to the threshold for the transition from aligned to perpendicular configuration determined by Malinen et al. (2016) in the L1642 high-latitude star-forming cloud, with $N_H \sim 1.6 \times 21$ cm^{-2}.

To investigate the relative orientation as a function of the evolutionary stage of the filaments more quantitatively, one would need to determine the linear mass of the filaments to assess whether they are supercritical or not. In our current study, supRHT is used to determine the direction of the filamentary structures but the method does not allow us to determine with accuracy the physical boundaries of the filaments and hence their linear masses.

However, focussing our analysis on a subsample of filaments for which we have a distance estimate (in the nearby clouds, at distances lower than 500 pc), we have shown that the change of relative orientation happens in the dense medium, with a transition in density around $n_{\rm H} \sim 10^3$ cm^{-3}. Although this value is approximate, it reveals that the formation of dense filamentary structure is affected by the cloud-scale magnetic field. This result and the transition value estimate are consistent with the recent analysis by Fissel et al. (2018) in Vela-C based on observations with BLAST-pol balloon-borne experiment and molecular lines tracing different gas densities.

(iii) At the clump scale:

We observe, for the densest clumps of our sample, a bimodal distribution of the relative orientation between the matter and the magnetic field in the filaments. This is similar to the findings of Zhang et al. (2014) in dense cores using SMA polarimetric measurements and James Clerk Maxwell Telescope (JCMT) continuum observations. Ching et al. (2017) showed that within massive cores the magnetic field structure is complex, in contrast to the ordered parsec-scale magnetic fields in the filament. They also find that the major axes of the cores are either parallel or perpendicular to the magnetic field of the filament, suggesting that the parsec-scale magnetic fields play an important role in the formation of massive cores providing support against gravity. Nevertheless, Poidevin et al. (2014) observed no preferential alignment between the distribution of cores observed with *Herschel* in the Lupus I region and the orientation of the magnetic fields on the parsec-scale derived from the BLAST polarimetric measurements.

We emphasize that the different relative orientations observed (perpendicular, parallel or no preferential) may be related to the variety of the clumps in terms of nature and evolutionary stage. The *Planck* clumps have been detected with a method using the colour signature of cold sources, and based on the detection of the cold residuals emission after removal of the warmer background (Planck Collaboration XXIII 2011b). Such a method results in the detection of extended cold components with a more complex morphology compared to methods identifying compact sources bright in their total intensity. The *Herschel* follow-up of a representative sample of 350 PGCCs (in the frame of the Galactic Cold Cores Key Programme) has revealed a rich and complex substructure within the *Planck* clumps, with sources at different evolutionary stages, from dense and cold cores (down to 7 K) to protostellar objects (Planck Collaboration XXII 2011a; Juvela et al. 2012; Montillaud et al. 2015). The *Planck* clumps, being elongated and more extended than the *Planck* beam, could be considered as a 'cold matrix' linking dense substructures to each other over a broad range of scales. More recently, the SCOPE JCMT legacy survey performed with the SCUBA-2 instrument at JCMT to map about 1000 PGCCs in 850 μm continuum emission has detected thousands of dense cores, identified as either starless cores or protostellar cores with young (Class 0/I) sources (Liu et al. 2016; Tatematsu et al. 2017; Juvela et al. 2018a).

6 CONCLUSION AND PERSPECTIVES

In this statistical analysis, our goal was to investigate whether the relative orientations in the POS between interstellar magnetic fields and filaments hosting *Planck* cold clumps may vary with the density of the environment and may also depend on the filaments evolutionary stage. For this purpose, we considered subsamples of filaments embedded in different background column densities and showing different density contrast with their environment. Furthermore, we drew a distinction between the area covered by clumps (clump area) and the remaining area of the filament (filament area).

Our main results are summarized below:

(i) Filaments versus background magnetic field:

(a) The filaments embedded in low-density environment, i.e. below $N_{\rm H,bkg} = 1.2 \times 10^{21}$ cm^{-2} (median value in our sample), show a clear parallel relative orientation with the background magnetic field (the upper panel of Fig. 5). However, while this preferential relative orientation is significant for the filaments with low-density contrast, it disappears for high-contrast filaments (the upper panel of Fig. 6).

(b) The filaments embedded in dense environment corresponding to column densities above $N_{\rm H,bkg} = 1.2 \times 10^{21}$ cm^{-2} do not globally show any preferential relative orientation with respect to the background magnetic field (the upper panel of Fig. 5).

(c) Our column density limit between parallel and perpendicular preferential relative orientation is close to the threshold values derived by Malinen et al. (2016) and Planck Collaboration XXXV (2016c) when using the same opacity as in our study ($1.6\,10^{21}$ and $2\,10^{21}$ cm^{-2}, respectively).

These results support the idea of a magnetic field strong enough to influence the formation of filaments. However, even if the low-density regions are mostly dominated by turbulence and magnetic fields, leading to preferential parallel alignments, self-gravity must play a significant role for the higher density structures. Although a perpendicular alignment is observed for low-density contrast filaments in high-density environment, no preferential relative orientation is prevailing for the high-contrast subsamples, whatever the density of their environment.

(d) In the clump areas, both perpendicular and parallel relative orientations are observed regardless of the environment column density (the lower panel of Fig. 5). However, in the low column density environment, the relative orientation turns from parallel to mostly perpendicular as one moves from the lowest to highest density contrast (the lower panel of Fig. 6). The finding indicates that the large-scale (background) magnetic fields play an important role not only during the formation of filaments but also of their embedded clumps.

(e) We also find that the relative orientation between the background magnetic field and the filaments strongly depends not only on the density but also on the nature of the structures such as the embedded clumps or the filaments excluding clumps.

(ii) Filaments versus their inner magnetic field:

(a) For the filaments, we find a preferential parallel relative orientation in both low- and high-density contrast subsamples that is consistent with the study from Planck Collaboration XXXIII (2016b). However, we note that for the high-density contrast filaments, the distribution is flatter (the upper panel of Fig. 8).

(b) For the clumps, in both subsamples, we also find preferential parallel relative orientation. However, in the high column density contrast subsample, there is a significant peak of the DF at angles larger than 70° that indicates perpendicular relative orientation (the lower panel of Fig. 8). This could be a signature of the presence of dense structures that were formed by contraction along the magnetic field lines with their major axes perpendicular to it.

(iii) Filament magnetic field versus background magnetic field:

(a) The magnetic fields in the background and in the filaments are mostly parallel to each other for the low column density contrast filaments. For the high column density contrast filaments, the parallel relative orientation between both fields is rare while globally we observe no preferential relative orientation (Fig. 10). This relative alignment depends also on the environment column density, being weaker for the filaments embedded in denser environments (Fig. C6). This could point to a coupling between the matter and the magnetic field during the filament formation process, as emphasized in the study by Planck Collaboration XXXIII (2016b).

(iv) Relative orientation in the nearby filaments:

We have looked for a possible correspondence between the relative orientation of filaments and magnetic fields (both background and inner) depending on the gas volume density using filaments of our sample with a distance estimate and associated to nearby molecular clouds.

(a) Filaments with densities larger (respectively lower) than $\sim$1200 cm^{-3} are mostly perpendicular (respectively parallel) with respect to the background magnetic field (Fig. 11).

(b) Densest clumps (densities larger than 2900 cm^{-3}) contribute to either parallel or perpendicular relative orientation with respect to the inner magnetic field while no preferential relative orientation is established for clumps with lower densities (Fig. 12). This could disentangle the similar behaviour observed in the clumps in the low and high column density environments, shown in the lower panel of Fig. 5. Denser clumps show tendency to be perpendicular to the filament magnetic field.

We emphasize that these values of volume densities are subject to limitations due to uncertainties in the distance estimates and to the assumptions on the filaments and clumps shape and geometry, and thus are only tentative values. However, these results show that the change of relative orientation happens in the dense medium, and that our transition value estimate is consistent with the recent analysis by Fissel et al. (2018) in Vela-C based on observations with BLAST-pol balloon-borne experiment and molecular lines tracing different gas densities.

This study brings information on the role of the magnetic fields in the evolution of the dense ISM matter at the intermediate scale between molecular clouds and dense cores. It reveals several regimes in the evolution of the filaments where the magnetic field is one of the dominant factors. Our results also indicate that the evolution of the filament with respect to its environment as well as the environment itself is the key in studying the role played by the magnetic field in structuring the matter, and can already be investigated with the *Planck* data. A dedicated analysis on known molecular clouds could bring new insights on the origin of the parallel or perpendicular alignment depending on the evolution of the clouds and/or efficiency of star formation in the clouds. We would like to emphasize that the contribution of the cold clumps should be considered in future studies of filamentary structures.

A more precise study of the interplay between matter and magnetic fields in the cold clumps at higher resolution could disentangle the dependence of the relative orientation on the geometry of the clump and of its evolutionary stage. Recent attempts in this field were performed with, e.g. the *Planck* follow-ups of the PGCCs with the SCUBA-2/POL-2 polarimeter at JCMT (Liu et al. 2018b; Juvela et al. 2018b). We have also started a statistical analysis of the polarization properties of a large sample of clumps from the PGCCs in order to investigate the dependence of the polarized emission with the column density, considering the respective impacts of the dust alignment efficiency and the magnetic field geometry (Ristorcelli et al. in preparation).

ACKNOWLEDGEMENTS

Funding from Ministry of Education and Science of the Republic of Kazakhstan state-targeted programme BR05236454 is acknowledged. Funding from Nazarbayev University ORAU grant SST 2015021 is acknowledged. DA and EA acknowledge the Nazarbayev University Faculty Development Competitive Programme (grant No. 110119FD4503). MJ and ERM acknowledge the support of the Academy of Finland Grant No. 285769. IR, KF, J-PB, and LM thank the support from the Programme National Physique et Chimie du Milieu Interstellaire (PCMI) of CNRS/INSU with INC/INP co-funded by CEA and CNES.

DA thanks Professor Anvar Shukurov for his suggestions on the statistical aspects of the study.

The authors thank the anonymous referee for the valuable comments that helped to improve the quality of the paper.

REFERENCES

Abergel A., Boulanger F., Mizuno A., Fukui Y., 1994, ApJ, 423, L59
Alves F. O., Franco G. A. P., Girart J. M., 2008, A&A, 486, L13
André P., Men'shchikov A., Bontemps S., Könyves V., Motte F., Schneider N., 2010, A&A, 518, L102
Di Francesco J., Ward-Thompson D., Inutsuka S.-I., Pudritz R. E., Pineda J. E., 2014, in Beuther H., Klessen R. S., Dullemond C. P., Henning T., eds, Protostars and Planets VI. Univ. Arizona Press, Tucson, p. 27
Beckwith S. V. W., Sargent A. I., Chini R. S., Guesten R., 1990, AJ, 99, 924
Berens P., 2009, J. Stat. Softw., 31, 1
Chapman N. L., Goldsmith P. F., Pineda J. L., Clemens D. P., Li D., Krčo M., 2011, ApJ, 741, 21
Chen C.-Y., King P. K., Li Z.-Y., 2016, ApJ, 829, 84
Ching T.-C., Lai S.-P., Zhang Q., Girart J. M., Qiu K., Liu H. B., 2017, ApJ, 838, 18
Clark S., Peek J., Putman M., 2014, ApJ, 789, 82
Cox N. L. J. et al., 2016, A&A, 590, A110
Crutcher R., 2012, ARA&A, 50, 29
Dotson J. L., Davidson J., Dowell C. D., Schleuning D. A., Hildebrand R. H., 2000, ApJS, 128, 335
Efron B., Tibshirani R. J., 1993, An Introduction to the Bootstrap. Chapman & Hall, New York
Falgarone E., Pety J., Phillips T. G., 2001, ApJ, 555, 178
Fissel L. M. et al., 2018, preprint(arXiv:1804.08979)
Franco G. A. P., Alves F. O., Girart J. M., 2010, ApJ, 723, 146
Goodman A. A., Myers P. C., Bastien P., Crutcher R. M., Heiles C., Kazes I., Troland T. H., 1990, Proceedings of the 140th Symposium of the International Astronomical Union, Galactic and Intergalactic Magnetic Fields. Kluwer Academic Publishers, Dodrecht, Netherlands, p. 319
Hennebelle P., 2013, A&A, 556, A153
Inutsuka S., Inoue T., Iwasaki K., Hosokawa T., 2015, A&A, 580, A49
Juvela M. et al., 2010, A&A, 518, L93
Juvela M. et al., 2011, A&A, 527, A111+
Juvela M. et al., 2012, A&A, 541, A12
Juvela M. et al., 2018a, A&A, 612, A71
Juvela M. et al., 2018b, A&A, 620, A26
Juvela M., Ysard N., 2012, A&A, 539, A71
Koch P. et al., 2014, ApJ, 797, 99
Könyves V. et al., 2015, A&A, 584, A91
Lee J.W.Y., Hull C.L.H., Offner S.S.R., 2017, ApJ, 834, 201
Li H.-B., Fang M., Henning T., Kainulainen T., 2013, MNRAS, 436, 370
Li H.-B., Goodman A., Sridharan T. K., Houde M., Li Z.-Y., Novak G., Tang K. S., 2014, in Beuther H. , Klessen R. S., Dullemond C. P., Henning T., eds, Protostars and Planets VI. Univ. Arizona Press, Tucson, p. 101
Liu T. et al., 2015, PKAS, 30, 79
Liu T. et al., 2018a, ApJS, 234, 28
Liu T. et al., 2018b, ApJ, 859, 151L
Liu T. et al., 2016, ApJS, 222, 7
Malinen J. et al., 2016, MNRAS, 460, 1934
Matthews T., 2013, PhD thesis, Northwestern Univ.
Matthews B. C., McPhee C. A., Fissel L. M., Curran R. L., 2009, ApJS, 182, 143
Men'shchikov A. et al., 2010, A&A, 518, L103
Miville-Deschênes M.-A. et al., 2010, A&A, 518, L104
Molinari S., Swinyard B., Bally J., Barlow M., Bernard J.-P., Martin P., 2010, A&A, 518, L100
Montier L., Plaszczynski S., Levrier F., Tristram M., Alina D., Ristorcelli I., Bernard J.-P., 2015, A&A, 574, A135
Montier L. A., Pelkonen V., Juvela M., Ristorcelli I., Marshall D. J., 2010, A&A, 522, A83
Montillaud J. et al., 2015, A&A, 584, 92
Motte F. et al., 2010, A&A, 518, L77
Nakamura F., Li Z.-Y., 2008, ApJ, 687, 354
Palmeirim P. et al., 2013, A&A, 550, A38
Pattle K. et al., 2017, ApJ, 846, 122
Pereyra A., Magalhães A. M., 2004, ApJ, 603, 584
Pilbratt G. et al., 2010, A&A, 518, L1
Planck Collaboration XXII, 2011a, A&A, 536, A22
Planck Collaboration XXIII, 2011b, A&A, 536, A23
Planck Collaboration XI, 2014, A&A, 571, A11
Planck Collaboration XIX, 2015a, A&A, 576, A104
Planck Collaboration XXVIII, 2015b, A28, A&A, 594
Planck Collaboration XXVIII, 2015c, A&A, 594, A28
Planck Collaboration XXXV, 2015d, 586, A138, A&A
Planck Collaboration XXXII, 2016a, A&A, 586, A135
Planck Collaboration XXXIII, 2016b, A&A, 586, A136
Planck Collaboration XXXV, 2016c, A&A, 586, A138
Planck Collaboration, 2018, A&A, Submitted
Poidevin F. et al., 2014, ApJ, 791, 43
Polychroni D. et al., 2013, ApJ, 777, L33
Price D., Bate M., 2008, MNRAS, 385, 1820
Rivera-Ingraham A. et al., 2017, A&A, 601, A94
Schneider S., Elmergreen B., 1979, ApJS, 41, 87
Soler J. D., Hennebelle P., 2017, A&A, 603, A64
Soler J. D., Hennebelle P., Martin P. G., Miville-Deschênes M.-A., Netterfield C. B., Fissel L. M., 2013, ApJ, 774, 128
Sousbie T., 2011, MNRAS, 401, 350
Stone J. M., Ostriker E., Gammie C., 1998, ApJ, 508, L99
Sugitani K. et al., 2011, ApJ, 734, 63
Tang Y.-W., Ho P. T. P., Koch P. M., Girart J. M., Lai S.-P., Rao R., 2009, ApJ, 700, 251
Tassis K., Dowell C. D., Hildebrand R. H., Kirby L., Vaillancourt J. E., 2009, MNRAS, 399, 1681
Tatematsu K. et al., 2017, ApJS, 228, 12
Ward-Thompson D., Kirk J., 2000, ApJ, 537, 135
Wu Y., Liu T., Meng F., Li D., Qin S.-L., Ju B.-G., 2012, ApJ, 756, 12
Zhang Q. et al., 2014, PASP, 792, 116

APPENDIX A: KERNEL DIMENSIONS TESTS

We test kernels of different sizes: $k_s = 11,\ 21,\ 31$ arcmin noted as K11, K21, and K31, respectively, and observe their effect on the detection of the filaments in the intensity minimaps. These selected sizes are motivated by the sizes of the elongated clumps and by the resolution of the data. K11 yields positive detection for Bok globules. K11 and K21 yield positive detections for cometary shape clumps. K31 is the most restrictive in detecting linear filaments that span in two directions from the centre of the minimaps. The kernel width $k_w = 6'$ is found to eliminate the round-shape isolated clumps. Larger widths do not allow us to detect the filaments at the position of the clumps because of the average size of the clumps, which is about $6'$. Resulting maps of I_{RHT} better reflect the variations of the structures compared to larger values of k_w, whereas smaller values are not appropriate as they do not allow us to take the clump width into account.

Table A1. Characteristicsofthe filaments used in the study. Columns: number in the PGCC catalogue, galactic longitude, galactic latitude, length, width, average position angle given by the SupRHT method using Gaussian fit, its uncertainty, average column density over the filament and its uncertainty, average column density over the filament excluding clumps areas and its uncertainty, average column density over the background region and its uncertainty, average magnetic field angle over the filament using Gaussian fit, average magnetic field angle over the filament using circular statistics and its uncertainty.

Number	l (deg)	b (deg)	s ($'$)	w ($'$)	$\langle\theta\rangle_{\rm fil,2}$ (deg)	$\sigma(\langle\theta\rangle_{\rm fil,2})$ (deg)	$\langle N_{\rm H,tot}\rangle$ ($\times10^{20}$ cm^{-2})	$\sigma(N_{\rm H,tot})$ ($\times10^{20}$ cm^{-2})	$\langle N_{\rm H,fil}\rangle$ ($\times10^{20}$ cm^{-2})	$\sigma(N_{\rm H,fil})$ ($\times10^{20}$ cm^{-2})	$\langle N_{\rm H,bkg}\rangle$ ($\times10^{20}$ cm^{-2})	$\sigma(N_{\rm H,bkg})$ ($\times10^{20}$ cm^{-2})	$\langle\psi\rangle_2$ (deg)	$\langle\psi\rangle_1$ [°]	$\sigma(\psi)_1$ [°]
27	1.395	20.933	92.0	11.0	84.0	1.0	20.9	13.2	17.9	6.71	20.9	13.2	N/A	N/A	N/A
54	300.797	−9.101	81.0	7.0	9.0	1.0	35.6	5.79	34.7	4.95	35.6	5.79	−71.0	−72.3	10.1
67	355.324	14.725	103.0	14.0	−57.0	12.0	66.0	13.0	63.9	11.5	66.0	13.0	N/A	N/A	N/A
75	161.671	−35.917	59.0	7.0	52.0	7.0	11.0	6.07	9.49	4.48	11.0	6.07	67.0	56.0	36.8
80	110.627	−12.496	60.0	7.0	60.0	4.0	11.2	2.18	10.7	1.65	11.2	2.18	56.0	48.3	30.3
86	110.418	11.532	55.0	6.0	24.0	2.0	25.5	5.51	23.2	3.37	25.5	5.51	29.0	25.7	21.0
88	301.267	−8.25	84.0	9.0	32.0	3.0	32.5	6.71	31.1	6.06	32.5	6.71	−68.0	−57.9	47.2
119	301.598	−7.834	55.0	8.0	34.0	5.0	31.3	7.37	33.2	7.57	31.3	7.37	−72.0	−59.9	50.7
124	28.46	−6.401	47.0	5.0	53.0	12.0	15.8	7.66	12.5	1.99	15.8	7.66	47.0	40.6	37.4
138	142.645	7.738	84.0	7.0	15.0	20.0	25.1	4.63	23.6	2.72	25.1	4.63	81.0	33.5	56.2
158	314.958	−21.971	90.0	8.0	20.0	5.0	10.3	3.33	9.36	2.65	10.3	3.33	38.0	36.6	38.2
185	140.983	5.733	43.0	6.0	−33.0	2.0	46.9	11.7	41.5	6.24	46.9	11.7	−64.0	−44.6	42.8
210	312.501	−22.741	77.0	9.0	42.0	12.0	10.0	4.37	9.39	3.82	10.0	4.37	27.0	26.8	6.0
219	7.657	21.185	50.0	7.0	52.0	22.0	27.0	7.44	23.6	3.94	27.0	7.44	−56.0	−35.6	47.5
233	205.458	−14.561	63.0	7.0	−36.0	6.0	82.8	38.4	75.5	35.4	82.8	38.4	−72.0	−30.5	64.7
235	325.567	6.034	48.0	7.0	7.0	5.0	25.9	10.7	23.5	10.6	25.9	10.7	N/A	N/A	N/A
238	159.412	−34.371	41.0	7.0	58.0	3.0	48.8	20.8	50.7	22.9	48.8	20.8	−50.0	−45.6	18.4
266	121.929	−7.668	52.0	7.0	36.0	13.0	20.0	3.16	19.1	2.5	20.0	3.16	−55.0	−50.9	24.7
366	317.275	6.132	49.0	4.0	13.0	11.0	26.3	8.67	21.7	7.16	26.3	8.67	19.0	22.8	25.6
403	298.318	−13.616	66.0	9.0	−201.0	50.0	15.3	6.62	13.8	5.49	15.3	6.62	−66.0	−8.5	53.5
448	160.528	−19.727	47.0	8.0	65.0	7.0	26.6	4.61	23.9	2.31	26.6	4.61	N/A	N/A	N/A
498	337.688	7.485	55.0	7.0	−26.0	12.0	27.2	7.68	23.5	5.04	27.2	7.68	78.0	55.7	46.6
504	173.118	2.355	53.0	6.0	75.0	4.0	93.5	23.7	83.9	17.4	93.5	23.7	N/A	N/A	N/A
516	201.717	−11.22	71.0	8.0	50.0	14.0	29.0	4.97	28.4	4.3	29.0	4.97	N/A	N/A	N/A
520	91.299	−38.159	70.0	10.0	−23.0	8.0	5.02	1.63	4.44	1.12	5.02	1.63	N/A	N/A	N/A
533	169.964	−18.991	88.0	7.0	17.0	12.0	29.2	10.6	27.5	9.59	29.2	10.6	−86.0	−41.4	59.4
562	28.714	3.882	66.0	6.0	73.0	2.0	176.0	73.9	138.0	33.9	176.0	73.9	N/A	N/A	N/A
633	127.882	2.675	74.0	8.0	−35.0	27.0	33.0	4.36	32.0	2.21	33.0	4.36	−64.0	−36.8	50.6
673	171.411	−17.376	86.0	7.0	52.0	6.0	40.6	15.7	41.7	16.9	40.6	15.7	53.0	47.9	24.3
680	158.225	−20.287	78.0	6.0	−16.0	6.0	78.6	57.9	78.8	60.1	78.6	57.9	N/A	N/A	N/A
684	202.364	2.504	77.0	8.0	−74.0	3.0	63.6	20.2	60.7	18.4	63.6	20.2	N/A	N/A	N/A
715	107.483	−9.376	37.0	12.0	46.0	4.0	13.1	2.93	12.7	2.65	13.1	2.93	57.0	50.6	38.3
747	117.871	−10.719	69.0	6.0	−190.0	43.0	4.94	0.646	4.85	0.608	4.94	0.646	28.0	22.0	42.7
748	220.738	−8.055	37.0	9.0	−32.0	2.0	31.1	6.37	35.5	6.11	31.1	6.37	−84.0	−61.8	58.0
751	93.614	−4.456	72.0	8.0	−45.0	11.0	49.3	18.9	40.1	19.2	49.3	18.9	N/A	N/A	N/A
790	82.369	9.768	44.0	4.0	−1.0	5.0	7.1	1.83	5.55	0.711	7.1	1.83	N/A	N/A	N/A
794	170.0	−16.132	74.0	7.0	73.0	8.0	68.5	18.6	69.0	19.2	68.5	18.6	N/A	N/A	N/A
830	159.517	3.252	75.0	6.0	−148.0	32.0	31.3	4.43	30.7	4.25	31.3	4.43	67.0	55.2	40.1
834	157.592	−8.898	74.0	6.0	−80.0	5.0	44.9	14.2	45.5	15.2	44.9	14.2	N/A	N/A	N/A
846	165.157	−7.566	82.0	6.0	67.0	10.0	33.6	8.86	32.5	8.66	33.6	8.86	88.0	39.2	70.6
852	100.328	14.847	73.0	9.0	67.0	7.0	16.1	3.42	15.9	3.54	16.1	3.42	−43.0	−42.6	11.8
895	154.957	−15.184	39.0	9.0	66.0	2.0	25.5	6.94	25.7	7.71	25.5	6.94	N/A	N/A	N/A
937	121.036	−9.959	72.0	7.0	80.0	5.0	9.29	3.23	9.25	3.35	9.29	3.23	−41.0	−21.9	48.1
943	157.242	−3.933	65.0	9.0	−56.0	7.0	28.1	5.63	27.8	7.02	28.1	5.63	−30.0	−23.3	36.2

Table A1 – *continued*

Number	l (deg)	b (deg)	s (′)	w (′)	$\langle\theta\rangle_{\rm fil,2}$ (deg)	$\sigma(\langle\theta\rangle_{\rm fil,2})$ (deg)	$\langle N_{\rm H,tot}\rangle$ ($\times10^{20}$ cm^{-2})	$\sigma(N_{\rm H,tot})$ ($\times10^{20}$ cm^{-2})	$\langle N_{\rm H,fil}\rangle$ ($\times10^{20}$ cm^{-2})	$\sigma(N_{\rm H,fil})$ ($\times10^{20}$ cm^{-2})	$\langle N_{\rm H,bkg}\rangle$ ($\times10^{20}$ cm^{-2})	$\sigma(N_{\rm H,bkg})$ ($\times10^{20}$ cm^{-2})	$\langle\psi\rangle_2$ (deg)	$\langle\psi\rangle_1$ [°]	$\sigma(\psi)_1$ [°]
966	27.709	−21.028	84.0	9.0	53.0	12.0	7.61	2.86	7.3	2.8	7.61	2.86	N/A	N/A	N/A
996	216.0	−15.978	92.0	9.0	45.0	8.0	43.5	21.5	42.8	22.7	43.5	21.5	N/A	N/A	N/A
1019	165.622	3.342	56.0	5.0	50.0	8.0	18.8	4.0	17.4	2.63	18.8	4.0	88.0	3.2	66.4
1025	9.833	21.5	86.0	7.0	53.0	2.0	16.9	4.88	16.6	4.87	16.9	4.88	17.0	12.2	34.7
1128	139.186	−3.289	66.0	6.0	−67.0	5.0	32.2	5.1	31.4	4.59	32.2	5.1	−19.0	−21.9	17.0
1136	317.678	−28.655	46.0	6.0	−33.0	7.0	5.68	1.13	5.24	0.557	5.68	1.13	−5.0	−12.5	34.2
1230	171.92	−15.66	70.0	3.0	84.0	1.0	43.6	12.9	43.2	13.0	43.6	12.9	−46.0	−11.8	49.7
1269	170.824	−15.913	75.0	8.0	70.0	6.0	48.4	13.1	48.2	13.6	48.4	13.1	N/A	N/A	N/A
1270	302.488	−4.706	63.0	12.0	13.0	3.0	18.8	3.79	16.9	1.6	18.8	3.79	N/A	N/A	N/A
1342	175.333	−10.828	35.0	5.0	−77.0	9.0	19.2	1.99	18.1	0.413	19.2	1.99	−10.0	−13.7	18.1
1466	7.548	4.261	79.0	8.0	14.0	7.0	25.1	5.26	24.1	4.46	25.1	5.26	36.0	36.2	16.3
1480	266.964	−4.641	35.0	8.0	−30.0	14.0	35.5	5.4	35.0	5.42	35.5	5.4	N/A	N/A	N/A
1496	58.039	3.037	62.0	7.0	2.0	5.0	40.0	5.98	37.9	5.06	40.0	5.98	27.0	30.8	19.1
1519	128.213	13.701	72.0	12.0	72.0	6.0	28.2	4.36	27.8	4.18	28.2	4.36	87.0	−20.6	60.7
1528	121.862	−8.766	79.0	7.0	23.0	7.0	10.8	2.21	10.2	2.05	10.8	2.21	−3.0	14.7	33.4
1535	185.412	−8.962	55.0	6.0	−63.0	9.0	15.5	3.2	15.5	3.37	15.5	3.2	N/A	N/A	N/A
1555	171.747	−15.627	70.0	5.0	84.0	1.0	44.1	11.2	39.1	8.4	44.1	11.2	N/A	N/A	N/A
1594	268.228	−3.238	68.0	10.0	44.0	8.0	48.9	9.21	46.5	6.4	48.9	9.21	N/A	N/A	N/A
1602	149.679	3.562	96.0	9.0	58.0	8.0	58.5	12.1	58.1	12.5	58.5	12.1	19.0	17.8	21.0
1669	26.839	6.787	51.0	5.0	48.0	4.0	43.0	8.05	39.8	5.12	43.0	8.05	−88.0	−22.3	64.9
1695	236.513	−4.999	50.0	8.0	−62.0	2.0	19.8	2.64	19.4	2.81	19.8	2.64	−82.0	−1.5	50.7
1759	311.356	−19.419	69.0	6.0	−88.0	5.0	4.85	0.968	4.29	0.344	4.85	0.968	−68.0	−46.0	46.2
1778	294.553	5.928	70.0	8.0	18.0	4.0	11.1	1.87	9.89	1.18	11.1	1.87	75.0	16.3	55.1
1789	204.562	−11.02	72.0	6.0	15.0	4.0	30.5	12.5	30.2	13.3	30.5	12.5	13.0	12.4	16.9
1835	124.843	−6.04	34.0	12.0	61.0	9.0	14.9	2.38	13.2	1.92	14.9	2.38	−53.0	−30.9	48.9
1846	156.729	35.137	54.0	6.0	68.0	4.0	3.42	1.07	2.53	0.502	3.42	1.07	67.0	41.4	45.2
1874	320.845	5.094	65.0	19.0	−5.0	27.0	18.7	1.61	18.5	1.37	18.7	1.61	−79.0	−31.5	59.2
1955	210.97	−19.329	75.0	19.0	75.0	6.0	133.0	48.1	134.0	51.3	133.0	48.1	N/A	N/A	N/A
1959	101.592	22.68	80.0	7.0	26.0	6.0	4.87	0.707	4.52	0.508	4.87	0.707	22.0	21.4	11.6
2048	181.842	−18.381	87.0	6.0	30.0	9.0	28.7	11.8	28.9	12.2	28.7	11.8	N/A	N/A	N/A
2050	111.153	−40.985	74.0	6.0	−80.0	5.0	2.23	0.707	2.15	0.651	2.23	0.707	−73.0	3.4	54.5
2176	10.381	3.167	62.0	8.0	−30.0	11.0	46.3	9.1	43.0	8.32	46.3	9.1	N/A	N/A	N/A
2212	264.449	5.545	77.0	6.0	−20.0	6.0	16.8	1.97	16.8	2.08	16.8	1.97	60.0	36.0	44.5
2246	301.148	−16.179	62.0	6.0	−78.0	4.0	19.1	7.96	20.1	9.06	19.1	7.96	N/A	N/A	N/A
2308	217.071	−16.255	45.0	10.0	65.0	10.0	17.8	3.62	15.4	2.85	17.8	3.62	−20.0	−22.1	13.3
2315	171.435	−4.45	69.0	5.0	−36.0	4.0	17.5	3.72	16.8	4.07	17.5	3.72	−28.0	−7.6	47.8
2346	222.834	−5.606	83.0	7.0	30.0	4.0	25.4	1.97	25.3	1.99	25.4	1.97	82.0	25.3	56.7
2465	219.551	−3.85	39.0	5.0	4.0	16.0	17.9	2.73	15.8	1.19	17.9	2.73	52.0	17.1	44.0
2511	147.822	6.124	66.0	8.0	−58.0	9.0	22.1	2.05	21.4	1.88	22.1	2.05	−87.0	−24.4	73.4
2531	336.453	2.827	71.0	6.0	−86.0	6.0	53.0	5.61	52.1	5.12	53.0	5.61	−17.0	−16.4	23.2
2539	94.629	−31.306	92.0	9.0	−49.0	29.0	4.63	1.11	4.66	1.13	4.63	1.11	−53.0	−42.7	33.9
2583	314.948	−19.129	51.0	7.0	66.0	4.0	3.18	0.415	2.93	0.143	3.18	0.415	85.0	17.3	65.2
2587	112.809	2.76	70.0	5.0	−77.0	3.0	53.1	14.0	52.6	14.3	53.1	14.0	N/A	N/A	N/A
2602	230.663	−10.392	85.0	7.0	−32.0	15.0	7.77	1.18	7.45	0.975	7.77	1.18	73.0	20.6	49.4
2614	7.666	−7.856	86.0	7.0	−63.0	8.0	12.8	2.03	12.8	2.08	12.8	2.03	N/A	N/A	N/A
2627	179.744	−2.625	73.0	11.0	47.0	13.0	34.0	5.6	33.5	5.54	34.0	5.6	46.0	30.7	45.2
2703	229.255	−4.656	54.0	4.0	−84.0	2.0	12.8	3.74	12.0	3.96	12.8	3.74	63.0	26.6	50.9

Table A1 – *continued*

Number	l (deg)	b (deg)	s ($'$)	w ($'$)	$\langle\theta\rangle_{\rm fil,2}$ (deg)	$\sigma(\langle\theta\rangle_{\rm fil,2})$ (deg)	$\langle N_{\rm H,tot}\rangle$ ($\times10^{20}$ cm^{-2})	$\sigma(N_{\rm H,tot})$ ($\times10^{20}$ cm^{-2})	$\langle N_{\rm H,fil}\rangle$ ($\times10^{20}$ cm^{-2})	$\sigma(N_{\rm H,fil})$ ($\times10^{20}$ cm^{-2})	$\langle N_{\rm H,bkg}\rangle$ ($\times10^{20}$ cm^{-2})	$\sigma(N_{\rm H,bkg})$ ($\times10^{20}$ cm^{-2})	$\langle\psi\rangle_2$ (deg)	$\langle\psi\rangle_1$ [°]	$\sigma(\psi)_1$ [°]
2710	202.033	2.85	56.0	17.0	−74.0	3.0	60.7	22.5	65.6	21.5	60.7	22.5	−56.0	−56.1	13.1
2760	144.957	4.62	42.0	7.0	18.0	9.0	27.0	1.7	26.8	1.35	27.0	1.7	32.0	35.8	17.1
2778	359.781	11.933	80.0	6.0	−71.0	8.0	18.3	3.7	18.5	3.82	18.3	3.7	−57.0	−4.7	53.5
2927	89.494	2.041	68.0	10.0	63.0	12.0	89.6	14.9	88.9	14.9	89.6	14.9	N/A	N/A	N/A
2953	309.837	−24.868	69.0	10.0	−65.0	8.0	3.69	0.48	3.56	0.364	3.69	0.48	−66.0	−63.7	22.7
2964	8.264	21.383	60.0	6.0	22.0	3.0	27.6	8.03	28.4	8.36	27.6	8.03	0.0	10.7	31.9
3115	103.313	−23.938	48.0	5.0	76.0	6.0	3.1	0.374	3.0	0.313	3.1	0.374	−78.0	−42.7	55.3
3133	65.317	−2.652	48.0	6.0	78.0	7.0	52.9	9.96	49.6	13.8	52.9	9.96	−51.0	−44.8	34.4
3134	23.384	10.052	54.0	7.0	−1.0	2.0	27.4	3.27	25.4	1.82	27.4	3.27	31.0	29.4	14.8
3148	298.036	5.975	47.0	7.0	−24.0	8.0	12.8	1.86	11.8	1.12	12.8	1.86	N/A	N/A	N/A
3182	289.848	−7.503	98.0	10.0	45.0	13.0	7.85	1.17	7.62	1.05	7.85	1.17	−82.0	6.9	55.1
3439	53.706	6.929	49.0	6.0	20.0	7.0	17.2	2.84	15.9	2.17	17.2	2.84	N/A	N/A	N/A
3488	129.124	20.312	71.0	9.0	66.0	9.0	6.52	1.24	6.48	1.33	6.52	1.24	74.0	60.6	38.2
3561	29.121	2.224	59.0	5.0	61.0	6.0	54.2	5.99	53.2	5.34	54.2	5.99	N/A	N/A	N/A
3570	115.528	9.004	71.0	9.0	43.0	10.0	20.1	2.78	19.7	2.71	20.1	2.78	37.0	39.9	14.7
3593	101.279	17.602	88.0	9.0	−37.0	4.0	12.2	2.69	12.4	3.07	12.2	2.69	−7.0	−5.6	27.6
3700	254.402	−3.935	71.0	12.0	51.0	14.0	29.2	4.18	29.4	4.24	29.2	4.18	−70.0	−51.0	45.9
3711	106.604	−19.538	51.0	6.0	−75.0	8.0	5.59	1.09	6.01	0.625	5.59	1.09	−66.0	−15.1	54.3
3749	187.089	−33.345	76.0	6.0	−14.0	6.0	9.51	0.81	9.4	0.76	9.51	0.81	N/A	N/A	N/A
3831	150.424	3.475	53.0	5.0	41.0	2.0	38.0	6.84	35.1	5.7	38.0	6.84	73.0	56.1	51.8
3888	158.791	3.374	51.0	6.0	−84.0	7.0	25.8	7.6	32.5	5.67	25.8	7.6	60.0	54.3	26.4
3907	118.001	16.754	49.0	8.0	57.0	6.0	5.77	0.741	5.36	0.418	5.77	0.741	−13.0	−18.4	41.5
3935	162.39	9.907	53.0	8.0	10.0	3.0	8.77	0.758	9.14	0.426	8.77	0.758	−69.0	−43.6	47.1
3987	170.1	−7.731	69.0	8.0	−71.0	5.0	25.3	4.39	25.2	5.05	25.3	4.39	−29.0	−15.8	36.0
4187	100.772	14.924	52.0	6.0	−61.0	4.0	9.89	1.45	9.73	1.65	9.89	1.45	−35.0	−29.6	32.6
4192	191.502	8.333	81.0	9.0	−69.0	8.0	7.17	2.01	6.32	1.4	7.17	2.01	78.0	7.3	52.3
4240	300.611	−2.901	38.0	3.0	−1.0	24.0	26.1	3.73	25.7	3.7	26.1	3.73	N/A	N/A	N/A
4258	168.081	−5.408	70.0	7.0	79.0	3.0	25.5	2.52	25.1	1.88	25.5	2.52	−84.0	−50.9	56.3
4272	113.039	16.309	39.0	4.0	4.0	4.0	15.1	3.21	13.2	0.919	15.1	3.21	14.0	13.6	7.5
4330	166.176	−16.496	63.0	9.0	−67.0	12.0	20.8	4.81	19.4	3.67	20.8	4.81	N/A	N/A	N/A
4397	2.244	3.387	75.0	7.0	−53.0	2.0	47.2	7.87	46.1	7.82	47.2	7.87	N/A	N/A	N/A
4406	2.432	14.73	79.0	6.0	−65.0	16.0	8.94	1.89	8.81	1.85	8.94	1.89	−69.0	−62.2	37.3
4503	155.301	−23.076	59.0	5.0	−191.0	42.0	6.97	1.62	7.2	1.74	6.97	1.62	N/A	N/A	N/A
4610	3.472	10.813	88.0	7.0	−60.0	6.0	9.58	1.57	8.98	1.28	9.58	1.57	−62.0	−28.2	53.3
4789	215.573	−15.685	38.0	5.0	−3.0	4.0	21.2	3.51	21.2	3.74	21.2	3.51	N/A	N/A	N/A
4806	168.421	−5.388	81.0	16.0	80.0	4.0	25.5	2.16	25.6	2.23	25.5	2.16	−64.0	−30.1	49.3
4838	160.261	−19.793	60.0	7.0	66.0	8.0	27.0	4.72	28.2	5.11	27.0	4.72	N/A	N/A	N/A
4957	159.174	−9.002	60.0	4.0	−80.0	4.0	24.0	1.62	23.7	1.3	24.0	1.62	N/A	N/A	N/A
5459	320.924	14.906	45.0	7.0	−1.0	4.0	4.28	0.62	4.0	0.512	4.28	0.62	0.0	−3.7	44.5
5482	212.171	4.301	69.0	7.0	2.0	3.0	12.9	1.36	12.7	1.41	12.9	1.36	N/A	N/A	N/A
5499	169.382	−3.89	61.0	12.0	−54.0	3.0	22.1	2.44	20.1	1.44	22.1	2.44	−56.0	−33.8	44.3
5601	110.211	10.254	69.0	9.0	−47.0	18.0	13.7	1.91	13.7	1.97	13.7	1.91	N/A	N/A	N/A
5688	105.836	4.713	67.0	6.0	0.0	12.0	32.4	7.16	31.3	7.45	32.4	7.16	−23.0	−23.0	23.6
5777	151.172	−10.066	75.0	7.0	84.0	1.0	6.79	0.804	6.66	0.725	6.79	0.804	−79.0	−30.2	57.3
5811	115.762	22.701	75.0	7.0	15.0	6.0	4.57	0.527	4.3	0.402	4.57	0.527	N/A	N/A	N/A
5849	291.473	−4.201	62.0	10.0	78.0	4.0	21.4	2.45	20.8	1.97	21.4	2.45	N/A	N/A	N/A
13203	281.768	−30.794	68.0	2.0	73.0	4.0	5.39	1.08	5.25	1.26	5.39	1.08	−19.0	−10.4	44.2

APPENDIX B: ESTIMATION OF UNCERTAINTIES

In order to properly estimate the uncertainties, we proceed to bootstrap on independent pixels that corresponds to pixels situated at the minimum distances of 7′ between each other, which is equal to the resolution of the data. This diminishes the number of the pixels used. Thus, there are only 3 per cent of the pixels considered in each bootstrap round. The histograms of uncertainties are calculated as the ratio of standard deviations of the 5000 realizations of bootstrap over the values in each bin of the corresponding histograms (σ_N/N). We have checked that the average bootstrapped DFs are compatible with the DFs obtained directly from the data.

APPENDIX C: EXTRA FIGURES

See Figs C1–C8.

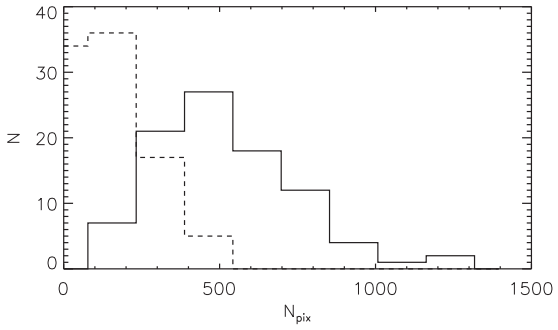

Figure C1. Histogram ofthe number of pixels ($N_{\rm pix}$) in the filaments only (solid line) and in the clumps only (dashed line).

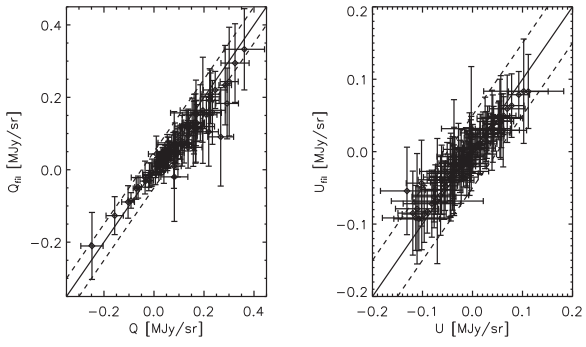

Figure C2. Scatter plot between the average Stokes parameters for each filament before and after the background subtraction in the filament pixels (Q is shown in the left panel and U is shown in the right panel). The error bars show the standard deviation in each filament. The lines show the one-to-one correlation and the dashed lines delimit 50 per cent variation.

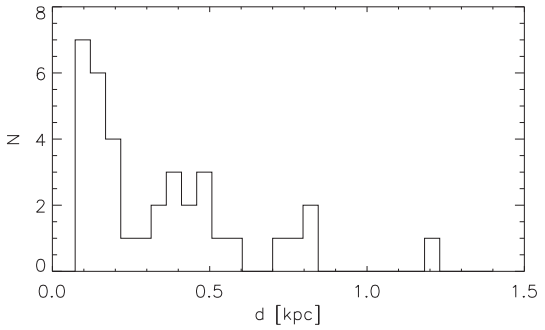

Figure C3. Histogram of the distances provided in the PGCC catalogue for the filaments used in our study.

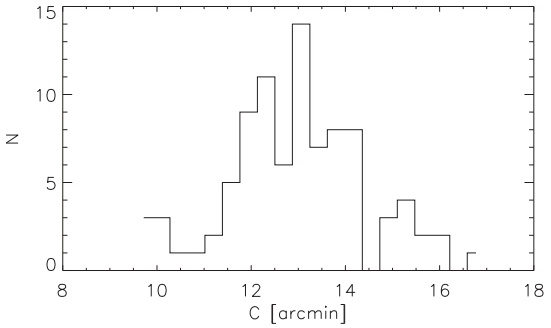

Figure C4. Histogram of the average clump sizes.

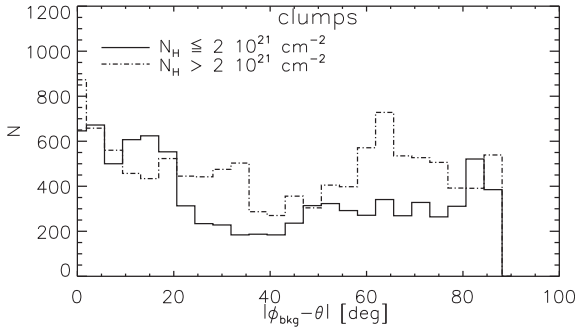

Figure C5. Histograms of absolute relative orientation between background magnetic field and orientation of the clumps for the clumps with densities lower and higher than 2×10^{21} cm^{-2} (solid and dash–dotted lines, respectively).

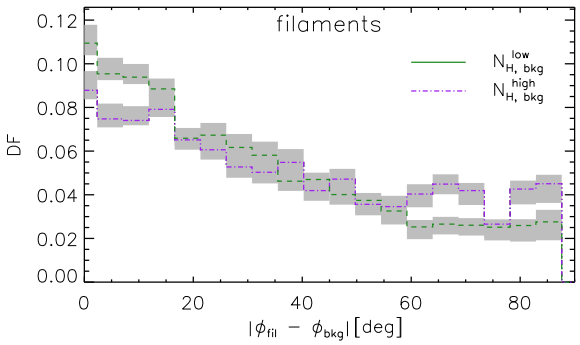

Figure C6. DF of the average difference between the magnetic field angles in the filaments and in the background. The green and purple lines show the DFs for the $N^{\rm low}_{\rm H,bkg}$ and $N^{\rm high}_{\rm H,bkg}$ subsamples, respectively. The uncertainties are shown as grey shaded areas.

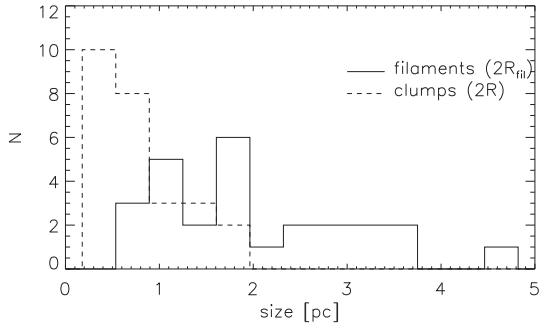

Figure C7. Histograms of the average clump size and filament width taken at the centre of the corresponding clump for the PGCCs with the distances lower than 500 pc.

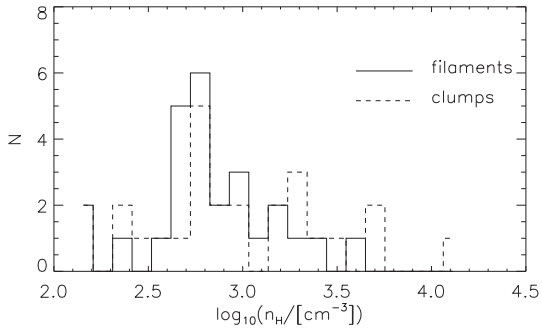

Figure C8. Histograms of the estimated mean gas volume densities for clumps (dashed line) and filaments (solid line) for PGCCs with distances lower than 500 pc.

This paper has been typeset from a TEX/LATEX file prepared by the author.